Diagnosis of Sheet Metal Forming Processes based on Thermal Energy Distribution - 3D Reconstruction

NG Yiu Ming

A Thesis Submitted in Partial Fulfillment
of the Requirements for the Degree of
Master of Philosophy
in
Automation and Computer-Aided Engineering

June 2005

Abstract

Sheet metal stamping process is a complicated process and it is widely used in automotive and aerospace industries. Today, owing to the ever-increasing demand for reduced production cost, sheet metal stamping operations are often pushed to the extreme (in terms of geometry shape, production speed, and etc.). This causes various problems such as tearing, wrinkling, excessive dimension variation, poor surface finishing and etc. In analyzing metal forming processes, comparison of the Finite Element Analysis (FEA) and the measured strain distribution is normally used. We can firstly use FEA to simulate the strain distribution of the deformed sheet metal stamping workpieces. Then we measure the experimental strain distribution of the sheet metal forming by the deformation of the test grid pattern, which is marked on the sheet metal blank at the beginning. By using this method, we are able to diagnose the stamping processes and eventually optimize the process and make the process closer to the limitations of the material properties.

In contrast, as the strain distribution and the thermal distribution in stamping processes are closely related, some researchers have simulated the thermal distribution from the strain distribution in metal forming processes recently. It shows similar characteristics in both the strain and the thermal distribution. Therefore, a novel diagnosis approach using thermal energy distribution can be used. This new approach is based on the fact that during the stamping process, the workpiece absorbs energy to deform. This is especially true for deep drawing

processes, as it generates a great amount of heat. Since most of the (plastic) deformation energy would be converted to heat energy, it is therefore possible to detect possible defects by means of analyzing its thermal energy distribution.

As it is impossible to put a number of temperature sensors on a workpiece right after stamped, instead, we take an infrared thermography and computer vision approach to measure the 3D experimental thermal distribution of a workpiece in sheet metal forming. With our new approach, we not only provide a new method to diagnose sheet metal stamping processes, but also give a new technology to acquire 3D thermal distribution of an object. Experimental results confirm the feasibility of our method. In this thesis, we firstly introduce the whole idea of our work. Then we describe the approach and the implementation of our diagnosis system. After that, the experimental results are shown and discussed. Finally, other possible applications and future research directions are given.

摘要

金屬片沖壓是一項複雜的過程。它在汽車和航空工業中廣泛使用。今天，由於減低生產成本的需求增加，金屬片沖壓操作經常被推至極限(在幾何形狀和生產速度等等)。這便產生了種種不同的問題，如撕破，皺褶，過分量度偏差和劣質表面處理等等。要分析金屬沖壓成形的過程，有限元分析和應變分佈測量的比較是經常被採用。我們首先用有限元分析去模擬變形後的金屬工件的應變分佈。然後再跟據預先刻上的點陣圖的變形去測量其真實的應變分佈。利用這方法，我們便可診斷金屬沖壓過程，做到優化過程和將過程推到材料特性的極限限制。

相反，由於應變分佈和熱力分佈是有著密切的關係，最近有一些研究員已將金屬沖壓過程的熱力分佈從應變分佈模擬出來。它展示了應變分佈和熱力分佈的相似屬性。因此，一個利用熱能分佈的新診斷方法便能使用。這個方法是基於在金屬沖壓過程中，工件吸收能量變形。這尤其適用於拉深過程，因它產生大量的熱力。由於大部份(塑性)變形會轉化爲熱能，因此我們能利用熱能分佈的分析去找出可能的毛病。

由於我們不可能將大量的溫度感應器放在一個剛剛沖壓出來的工件上，所以我們便結合紅外熱能圖像技術和計算機視覺技術去測量實際金屬沖壓工件的三維熱能分佈。我們不僅提供了一個診斷金屬沖壓過程的新方法，我們還提供了一個攝取物件的三維熱能分佈的新技術。實驗結果証實了我們的方法的可行性。這論文中，我們首先講述整個診斷方法的概念。其次，我們將描述我們的方法和診斷系統的實施。跟著，我們會展示和討論實驗結果。最後，我們會給出其他可能的應用和未來研究的方向。

Acknowledgments

I would like to sincerely thank my advisor, Professor Ruxu Du of The Chinese University of Hong Kong, for his continuous guidance, support, and encouragement over the past two years, my research project direction and work become clear and clear. Furthermore, he has taught me that the patience and work habit are very important to do research. I shall never forget his teaching.

Moreover, I would like to greatly thank Prof. Kwan–Yee Kenneth Wong from the University of Hong Kong for his invaluable comments on computer vision. I have benefited a lot from his comments and technical support.

Besides, I thank Mansfield Manufacturing Co. Ltd and Innovation and Technology Commission for the support of funding in this project. In addition, I sincerely thank Mr. Sam S. S. Lai from King Siu Metal Product Factory Ltd. for allowing us to conduct experiments in his factory.

Finally, I would like to thank some of the professors and colleagues. They are Prof. Ronald Chung, Prof. Yeung Yam, Prof. Youfu Li, Dr. G. C. Zhang, Dr. X. Wu, Allan Mok, Maolin Yu, Y. Huang, Simon Tong, Raymond Lam and Turkey Kwok for their comments, supports and discussions. I really enjoyed working in e-Manufacturing Laboratory for the past two years. It allowed me to work and study in a multi-cultural environment as well as to take part in various kinds of international conferences and seminars. I wish all the best for the growth and expansion of e-Manufacturing Laboratory.

Yiu-Ming Harry Ng

Contents

List of Figures

1. Introduction

Sheet metal stamping is one of the most common manufacturing processes. Everyday, millions of parts are made by stamping operations ranging from small battery caps to large automobile body panels. As a result, even a small technological advance may add to a significant corporative gain. It is well known that a sheet metal stamping process is a complicated process and it is associated to some forty process variables [1]. Basically, these variables can be classified into four categories: 1) workpiece characteristics (material property, thickness, geometric shape and dimension, and etc.); 2) die characteristics (surface finish, cleanness and etc.); 3) press characteristics (punch velocity, vibration modes and etc.); and 4) interaction variables (shot per minute, lubrication, and etc.). A stamping operation is completed in a very short period of time with a very large force causing elastic and plastic deformations, material hardening, micro-crack, macro-crack, thermal generation and etc. As a result, in practice, many problems may occur, such as wrinkling, necking (and subsequently tearing), scratching and orange peel. When failures occur, diagnosing the root cause(s) of the problem is very important.

One of the major problems in sheet metal stamping is die tryout: the time for a large die tryout could be several days. We can separate several stages in the problem analysis. They are improper design, improper making and improper operation. For improper design, it can be helped by means of Finite Element Modeling (FEM). For improper making, such as machining inaccuracy and

assembly error, these kinds of problems cannot be easily detected. For improper operation, such as poor lubrication, workpiece feeding not synchronizing and punch speed too high, this problem also cannot be easily detected.

In general, die try out and diagnosing the sheet metal stamping processes can be done using two types of methods: Finite Element Analysis (FEA) and experimental testing. With over thirty years of development, FEA is now a mature technology for analyzing sheet metal stamping operations. Today, it is a common practice for metal manufacturing companies to apply FEA in their product design and production control [2]. In fact, it has become a standard practice in the industry. There are several specialized commercial FEA software systems available, such as DYNAFORM©, PAM-STAMP© and AutoForm©. The main emphasis of the FEA is the formability. It gives the so-called Forming Limit Diagram (FLD), through which, one can predict possible defects, such as excessive thinning, fractures, or wrinkling.

Basically, a FEA system consists of three parts: a pre-processor, a solver and a post-processor. The pre-processor conducts meshing and setting up the boundary conditions. Automatic meshing, adaptive meshing, and user friendly interface are typical research topics in this area. The solver is the engine of the system that finds a numerical solution for the problem. The Moving Least-Squares Approximation algorithm and the Reproducing Kernel Approximation algorithm are the most recent development [3]. Its algorithm will determine the accuracy and the speed of the simulation. Due to the nonlinear nature of the sheet metal stamping, an iteration procedure is used to ensure equilibrium. It involves

repeated solutions in equations of large systems.

Another active research area is to combine FEA with varies kinds of optimization techniques to automatically obtain the optimum forming parameters and design specifications. Design of sensitivity [4]-[6], Response Surface Methodology (RSM) [7], [8] and Inverse Modeling Analysis [9] are preferred method used in sheet metal forming.

Once the tooling is designed and made, the tryout of the die will largely depends on the skilled machinists. FEA does help a lot in reducing die tryout time but it cannot fully replace the physical tryout because

(a) Metal forming theory are basically empirical, current FEA package based on one or other kinds of plastic theory are inherently imprecise.

(b) Metal forming process is a complex process that only a part of problems in stamping are addressable through simulations. Some variables like friction conditions, press speed profiles and material properties are usually idealized, and the actual values may be different from what we assumed.

Therefore, the actual results will have discrepancies with the simulated results. As FEA results cannot determine actual values in reality, experimental testing plays an important role in die tryout and diagnosis of sheet metal stamping processes.

In additional to the normal material tests, such as uniaxial tensile test, plane strain tensile test, Marciniak biaxial stretching test, hydraulic bulge test, Marciniak in-plane sheet torsion test, Miyauchi shear test, and various hardness tests [10], there have been a number of experiments designed to test the

formability in sheet metal stamping. These include Ericksen test, Olsen test, Fukui test, and Swift test [10].

Recently, with the rapid advancement of computer vision, strain analysis can be implemented, especially for deep drawing. The optical strain analysis system, GMO, is shown in Fig. 1.1 [11, 12].

Fig.1.1 GMO optical strain analysis system [11]

Basically, the working procedures consist of three steps. First, before the stamping, the workpiece is marked with an array of evenly spaced dots. Note that after the stamping operation is carried out, as shown in Fig. 1.2, the dots must still be on the surface of the workpiece. Next, based on several images from different viewpoints, the 3D geometry of the workpiece is constructed. At this time, the deformation of the dots will show how the workpiece is being deformed and the experimental 3D strain distribution of the workpiece can be reconstructed. Fig. 1.3 shows their diagnosis method in sheet metal stamping. They initially model the

strain distribution of the workpiece in ideal situation from FEA. After that, they reconstruct the experimental 3D strain distribution of the workpiece after the stamping process using the deformation of the dots. At this time, they can compare the ideal strain FEA with the experimental strain from the deformation of grid pattern so as to perform diagnosis and find out the abnormal regions.

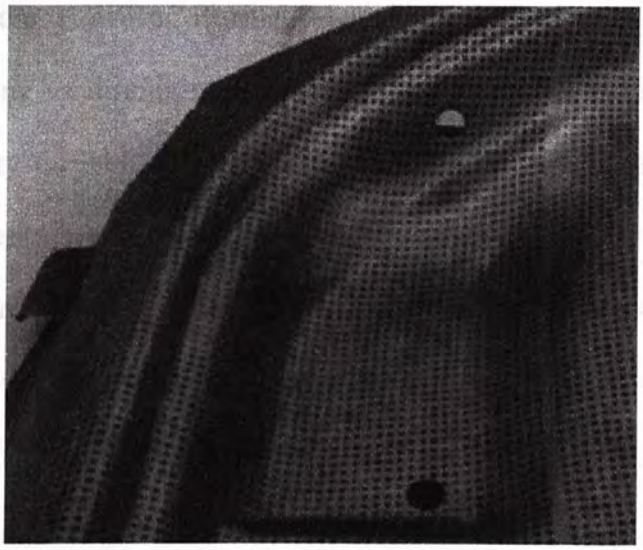

Fig.1.2 Shaped workpiece after stamping operation [11]

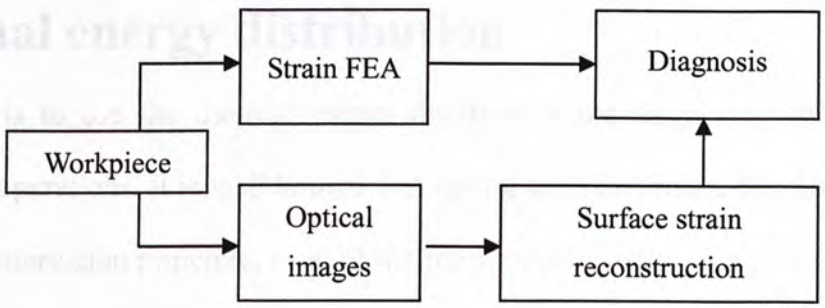

Fig.1.3 Block diagram of GMO's diagnosis method

While this method is accurate (the accuracy can reach up to 0.1 of dot spacing), it suffers from a time consuming procedure for marking grids. A similar system is

reported in [13], which uses a graphite spray to obtain the dots with a stochastic pattern. This is easier than the traditional electrochemically etching or laser etching. However, it still takes a lot of time in initial grid preparation.

In summary, modern FEA has become an industrial standard today and it is very effective and cost effective, as it can analyze the stamping operation without even building the die. However, it usually has an error about 10 ~ 20% because some of the stamping conditions, such as the speed of the press and the lubrication of the die, are very difficult to model. The experimental methods, such as the optical measurement, are very accurate and useful; but require a very time consuming preparation (i.e., marking the workpiece). As a consequence, it motivates us to develop a new method that uses the thermal energy distribution of the workpiece to diagnose sheet metal stamping operations.

1.1 Diagnosis concept based on thermal energy distribution

The idea is to use the thermal energy distribution for diagnosing sheet metal stamping operations. It is well known that during the sheet metal forming, by the energy conservation principle, most of the plastic deformation energy is converted into the thermal energy and thus generates heat, especially for deep drawing [5], [14]. Therefore, the characteristics of strain distribution of a workpiece can be represented by thermal energy distribution as well. In our method, it avoids the time consuming grid preparation. Fig. 1.4 shows our diagnosis concept in sheet

metal stamping. We initially compute the thermal energy distribution of the workpiece in ideal situation from strain FEA.

After that, we use an infrared camera to take several thermal images right after the stamping process in order to get the thermal distribution of the workpiece. At this time, we can compare the ideal thermal FEA with the experimental thermal distribution in order to diagnose the stamping process and find out the abnormal regions. In this approach, we not only save the time consuming preparation of initial grid pattern, but also eliminate the computation of experimental strain distribution from the deformation of grid pattern. This is because we can directly obtain the surface thermal distribution from thermal images. Normally, several 2D thermal images are sufficient to diagnose the stamping processes. However, if the workpiece is complicated, we may also reconstruct the 3D thermal distribution of the workpiece from a sequence of thermal images. As this method is designed to pin-point where the problem is, but not for online applications like monitoring, time (fast enough to keep up with production) is not a concern. Indeed, it allows a new tool (i.e. thermal distribution) for trained engineers to diagnose sheet metal stamping problems that cannot be seen before.

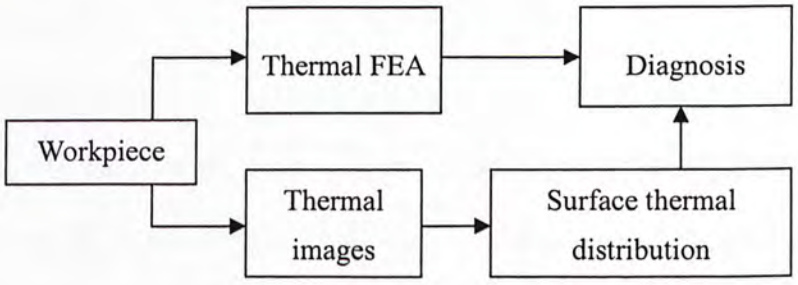

Fig.1.4 Block diagram of our diagnosis method

1.1.1 A cup drawing example

In this subsection, we give a comparison of the simulation result and the experimental result of a cup drawing. Cup drawing is a classical example of deep drawing. The studies of the deep drawing of cups can be dated back as early as 1920's [22] when the plastic deformation theory was just taking the shape. Later, much research has been conducted as shown in [23]-[27]. This is because of the following reasons:

(a) The symmetric shape of the part makes it easy to study.

(b) There are many factors that may affect the quality of the part.

(c) There are many practical products, such as the soft drink can and battery cap, that are really manufactured by this process.

However, if the drawing of a workpiece is deep, such as the deep drawing cup, we have to reconstruct the 3D thermal distribution of the stamping workpieces from several thermal infrared images right after the stamping operation [28]. This can provide a more realistic result for better observation, analysis and comparison with the thermal FEA. Fig. 1.5 shows the deep drawing cup (diameter is 120mm). Fig. 1.6 shows a simulation result of rise of temperature distribution of a cup drawing from FEA.

For this deep drawing cup, we use 18 thermal images to acquire its 3D thermal distribution. We take a total of 18 thermal images over a turntable sequence with 20 degree interval between each image. Fig. 1.7 shows the 3D thermal distribution of the deep drawing cup. When we compare it with the thermal FEA in Fig. 1.6,

we can see the similarity. Thus, we can conclude that the stamping process in deep drawing cup is satisfactory.

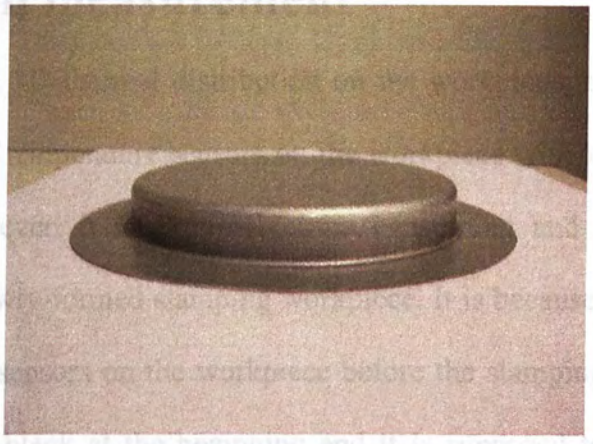

Fig.1.5 The deep drawing cup

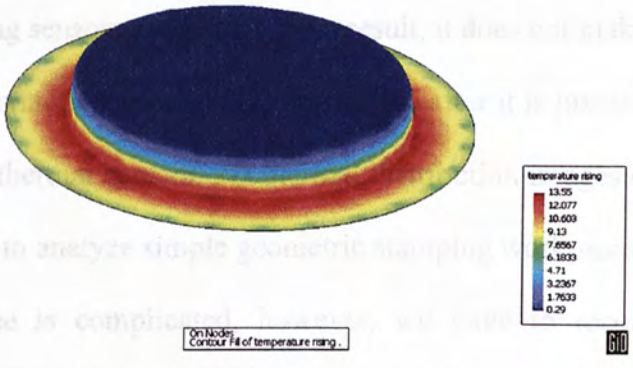

Fig.1.6 Thermal FEA result of the drawing cup

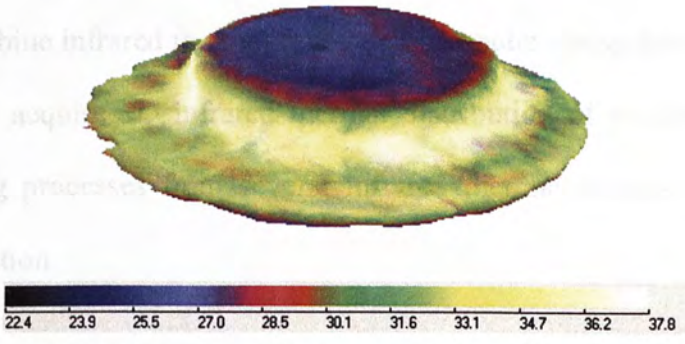

Fig.1.7 3D thermal distribution of the deep drawing cup

1.2 Need for 3D infrared thermal distribution measurement

In order to have a 3D thermal distribution on the workpiece, the best way is to place a number of temperature sensors on the workpiece with known position of each sensor. However, it is extremely time consuming and even impossible, especially for a newly-formed stamping workpiece. It is because we are unable to place temperature sensors on the workpiece before the stamping process, as it is just a sheet metal blank at the beginning and it is supposed to be fed into the stamping machine. Also, the temperature on the workpiece will be faded out after the time consuming sensors placement. As a result, it does not make sense to place a number of temperature sensors on the workpiece after it is just stamped. Instead, by using infrared thermal camera, 2D thermal distribution images can be obtained and it can be used to analyze simple geometric stamping workpieces.

If a workpiece is complicated, however, we have to reconstruct the 3D geometric shape and the thermal distribution of the stamping workpiece. Therefore, 3D infrared thermal distribution measurement is necessary. In this thesis, we combine infrared thermography and computer vision knowledge [29] to experimentally acquire 3D infrared thermal distribution of workpieces in sheet metal stamping processes from several infrared thermal images right after the stamping operation.

1.3 Outline of the Thesis

This thesis contains 10 chapters. The following chapters are organized as follows.

Chapter 2. Approach: This chapter firstly reviews the existing methods of acquiring 3D thermal distribution of objects. It then gives advantages and disadvantages of these methods. Finally, it describes what our approach to acquiring 3D thermal distribution in sheet metal stamping is, what the advantages over the existing methods are, and how we tackle the technical problems in our approach.

Chapter 3. Implementation of the Diagnosis System: In this chapter, it briefly describes the basic principles on thermograph acquisition. Then it shows the diagnosis system setup. Basically, it consists of an infrared camera, a tripod, a turntable and a net-and-board calibration box. After that, the perspective camera model is described. It is used to model the infrared camera in calibration and reconstruction. Next, it discusses how we calibrate our diagnosis system that involves an infrared camera. It introduces our proposed net-and-board calibration box for infrared camera calibration as traditional checkboard cannot be seen by infrared cameras. Finally, the reconstruction algorithm octree carving technique [30] is discussed.

Chapter 4. Consistency from Different Viewpoints: This chapter describes the experimental setup for ensuring the acquisition environment where consistency of temperature from different viewpoints is achieved. Basically, a validation resistor

box is made. Then a set of infrared thermal images are taken. The results show our acquisition environment is in an omni-directional infrared environment (there is no additional heat source that is affecting the thermal images captured by the infrared camera) and it is ready for temperature acquisition.

Chapter 5. Visual Reconstruction of Objects: In this chapter, visual images are used to reconstruct visual models based on the reconstruction algorithm "octree carving technique" described in chapter 3. A digital visual camera is used in the experiments. In these experiments, the visual reconstruction models are used for realistic perceptions. A "Siu Sun" cartoon model and a stamping disc are used as examples for illustration.

Chapter 6. Thermal Distribution Reconstruction of Stamping Workpieces: This chapter shows the results of 3D thermal distribution of stamping workpieces from infrared thermal images solely. The reconstruction algorithm is the one described in chapter 3. A digital infrared thermal camera is used in these experiments instead of a digital visual camera in chapter 5. The results confirm the feasibility and effectiveness of our proposed method in acquiring 3D thermal distribution from infrared thermal images of sheet metal stamping. Three stamping workpieces are used as examples. They are an air conditioner cap, a deep drawing cup and a stamping cylinder.

Chapter 7. Infrared Camera on a Robotic Arm: In this chapter, the infrared camera is mounted on a robotic arm for thermal image acquisition. As we can

calibrate any positions and any orientations before taking thermal images of an object, it allows arbitrary viewpoints for thermal image acquisition rather than a pure circular sequence described in chapter 6. The system is described and a teapot is used for illustration. Also, a comparison between the reconstruction from a circular sequence and the reconstruction from arbitrary viewpoints is shown.

Chapter 8. Compensation of Temperature Fade-out Problem: This chapter explains the problem of temperature fade-out and how the problem affects the 3D thermal reconstruction result. Temperature fade-out means the gradual decrease of the temperature on an object due to heat loss to the surroundings and heat conduction within an object. In this chapter, it also describes how we can solve the problem.

Chapter 9. Other Applications: In this chapter, other possible applications in industries are discussed. It is especially beneficial to automotive industry and general heat transfer analysis. Experimental verification with heat transfer Finite Element Analysis (FEA) results could be carried out in industries. The 3D thermal reconstruction result of a car body is shown.

Chapter 10. Conclusions: This chapter presents a summary on this thesis. It describes the main ideas from the need and the motivation of this project to the approach of the problem, from the implementation of the system to the experimental results, and from the compensation of temperature fade-out problem to the other application areas. Then the main contributions of the thesis are listed.

It consists of the implementation of the diagnosis system for sheet metal stamping, the proposal of net-and-board calibration box for infrared thermal cameras, the breakthrough of 3D thermal distribution acquisition from thermal images alone, the suggestions on the compensation of temperature fade-out problem, and the study of application in automotive industry. Finally, it concludes with possible areas for future research.

2. Approach

In the diagnosis of sheet metal stamping processes, there are several parts that we have to consider. They are the similarity and extreme temperature analysis, the thermodynamics for FEA in sheet metal stamping and the acquisition of 3D infrared thermal distribution of sheet metal stamping workpieces from infrared thermal images. In this chapter, it briefly discusses these three different parts. For the rest of this thesis, it focuses on the acquisition of 3D infrared thermal distribution of sheet metal stamping workpieces form infrared thermal images.

2.1 Similarity and extreme temperature analysis

Basically, a symmetric workpiece should give a symmetric strain distribution. It means that it should also give a symmetric temperature distribution. If we simply found that the temperature distribution of a workpiece right after stamping is asymmetric, we can easily identify these asymmetric regions. Moreover, as we can compute the ideal thermal FEA for a workpiece from its strain FEA, we can also compare the ideal thermal FEA with the experimental thermal distribution of the workpiece right after stamping using an infrared camera. Ideally, they should have similar characteristics in their distributions. That is the hottest region from the thermal FEA should be consistent with the hottest region in the experimental thermal distribution. If the distribution is not the same, we can localize the

locations of the abnormal regions on the workpiece and thus diagnose the stamping process. In addition, by analyzing the temperature values, we can also know whether the problematic region is over stressed or under stressed. This can particularly help skilled machinists to adjust the tools and dies as well as the stamping processes parameters.

Fig. 2.1 shows the progressive stamping workpiece. For these kinds of shallow stamping workpiece, one or two 2D thermal infrared images on top of it are already enough. Fig. 2.2 shows the thermal distribution of the progressive workpiece in Fig. 2.1. From Fig. 2.2, by using extreme temperature analysis, we can clearly see that there is a high temperature spot (in white color). Intuitively, it indicates that the bending of the location pin causes additional friction as a result of an asymmetric temperature distribution on the workpiece and extraordinary workpiece deformation. Thus, we can find out the problem, i.e. the dies are not manufactured with sufficient accuracy at that region. As a result, a part may be pushed out of the position and causes dimension deviation.

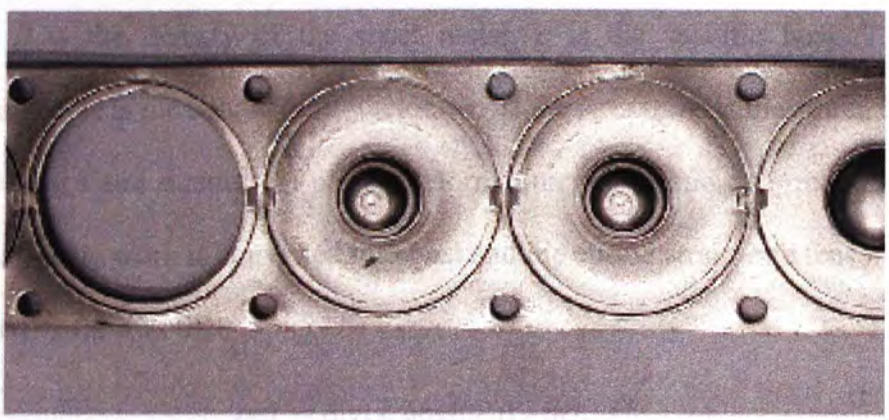

Fig.2.1 The progressive stamping workpiece

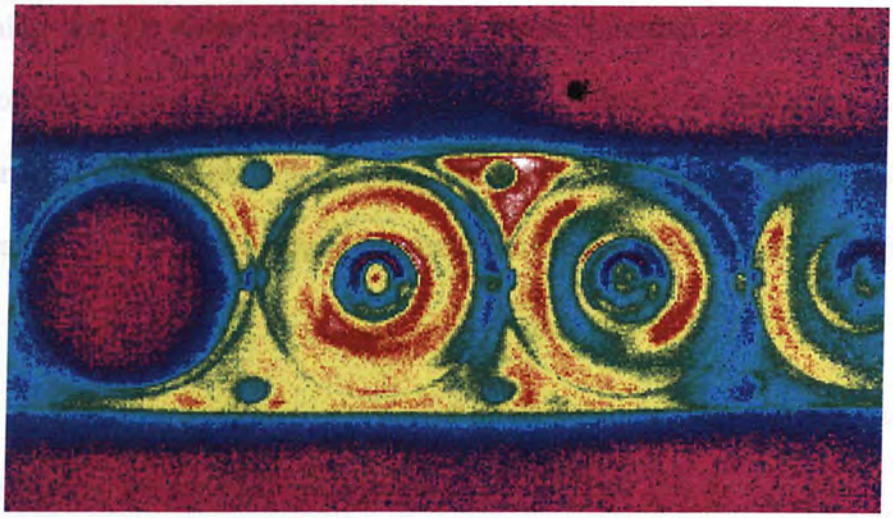

Fig.2.2 Thermal distribution of the progressive stamping workpiece

2.2 Thermodynamics for FEA in sheet metal stamping

The basic principle of heat generation in metal forming has been studied in [15, 16]. Briefly, it follows the equation below:

$$\rho c\dot{T} = \mathrm{div}[k.\mathrm{grad}(T)] + \sigma : \dot{\varepsilon}^p + T\frac{\partial \sigma}{\partial T} : \dot{\varepsilon}^e \qquad (1)$$

where, ρ is the density of the sheet metal, c is the specific heat, T is the temperature, k is the conductivity factor, σ is the stress, ε is the strain, and the superscripts p and e represent plastic deformation and elastic deformation. Since only the plastic work is converted into heat and the elastic strain-rate tensor can be neglected, it follows that:

$$\rho c\dot{T} = \mathrm{div}[k.\mathrm{grad}(T)] + \eta\sigma : \dot{\varepsilon}^p \qquad (2)$$

where $\eta \approx 0.9$ is a constant representing the fraction of work converted to heat.

Assuming that the sheet metal stamping process is carried out at a rapid speed (e.g., over 60 shots per minute), the heating is locally adiabatic, i.e. no heat transfer takes places with tools, dies and lubricants during the stamping. Thus, the temperature rise, ΔT, can be approximated by the following equation [17, 18]:

$$\Delta T = \frac{\eta}{\rho c}\int_0^{\Delta\bar{\varepsilon}} \bar{\sigma} d\bar{\varepsilon} \tag{3}$$

where $\bar{\sigma}$ and $\bar{\varepsilon}$ are effective stress and effective strain, respectively. Suppose that the material property follows the simple power law:

$$\bar{\sigma} = K\bar{\varepsilon}^{n} \tag{4}$$

and stress flow is a constant, then

$$\Delta T = \frac{\eta}{\rho c}\frac{K\Delta\bar{\varepsilon}^{(1+n)}}{(1+n)} \tag{5}$$

where, K is the stress flow constant [19]. According to the experiments on simple tensile testing [20], when the strain rate is greater than 10^{-2}/s with the total elongation 30% within 30 seconds, it fits the experiment data well in (5). It also shows that when necking occurs, the temperature rises quickly [21].

When considering the heat convection and conduction at the beginning (before stamping), the heat convection and conduction processes of the initial blank are stationary, then (2) becomes [19]:

$$\rho c\dot{T} = \mathrm{div}[k \cdot \mathrm{grad}(T)] - 2\frac{h}{t}(T - T_{air}) \tag{6}$$

where, h is heat convection coefficient, t is the thickness of the sheet, and T_{air} is the environment temperature (temperature of the air). In general, there might not be an analytical solution to (6), and hence, numerical methods must be used by (5).

We use the above equations to model the thermodynamics in sheet metal stamping processes and then find out the raise of temperature of a workpiece from the strain FEA. Fig. 1.10 shows the strain FEA of a workpiece and Fig. 1.11 shows its corresponding generated heat distribution by the above thermodynamic equations.

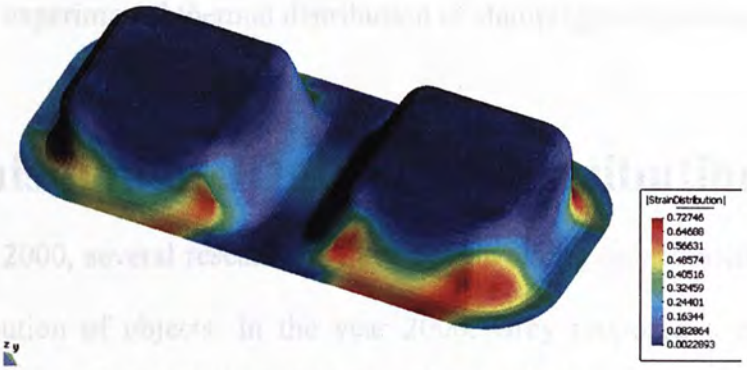

Fig.2.3 FEA equivalent strain distribution

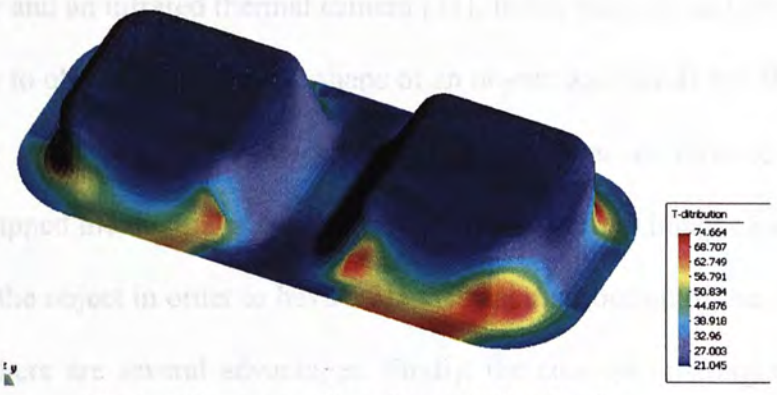

Fig.2.4 Corresponding thermal distribution

It should be pointed out that we only consider the raise of temperature in this case. In other words, the heat transfer within a workpiece by conduction and the heat loss to the surroundings are not considered. In reality, the temperature of a workpiece is changing over time, as the heat transfer and the heat loss are carried out from time to time. Therefore, future research can be carried out on the

modeling of time-variant thermal FEA for a workpiece in sheet metal stamping processes. From Fig. 1.10 and Fig. 1.11, we can clearly see the similar characteristics and distribution of the workpiece. The higher the strain at a certain region, the higher the temperature in that region is. Therefore, it motivates us to investigate the experimental thermal distribution of stamping workpieces.

2.3 Acquisition of 3D thermal distribution

Since the year 2000, several researchers have been working on acquisition of 3D thermal distribution of objects. In the year 2000, Gray proposed a method to acquire 3D thermal distribution of objects by combining the information of a 3D range scanner and an infrared thermal camera [31]. In his method, he firstly used a range scanner to obtain the geometric shape of an object, and that is the 3D model. He then took a set of thermal images of the object from an infrared camera. Finally, he mapped the thermal signature texture of the thermal images back to the 3D model of the object in order to have a 3D thermal distribution of the object. In his method, there are several advantages. Firstly, the concept is straightforward. Secondly, the 3D range scanner does provide an accurate and detailed geometric shape of the object. However, by using this method, there are several disadvantages. Firstly, 3D range scanners are extremely expensive. It costs about US$40,000 a piece. Secondly, there is a problem of template/texture fitting from 2D images to a 3D model. Actually, there is a large error in mapping 2D images to a 3D model without position and orientation configuration calibration between the

3D model and the thermal images. Without the configuration calibration, finding out the thermal signature by projection can not be done and the problem of point-to-point geometric warping from 2D plane to 3D model needs to be solved. Indeed, the point-to-point warping (template/texture fitting) is difficult. It is a research topic in computer graphics and it involves computational geometry and differential geometry problems. Therefore, the thermal signature of the 3D model might not be the exact region where the thermal signature is in reality.

In the year 2003, Nebel proposed a method to acquire 3D thermograms of a human face [32, 33]. He used a pair of stereoscopic cameras for acquiring geometric information of the objects and an infrared camera for acquiring thermal signature information. By using this method, it does not need a 3D range scanner and thus reduces the cost of the system. Also, since the stereoscopic cameras and the infrared cameras are calibrated with geometric configuration. It does not need to solve the template/texture fitting problem from a 2D plane to a 3D model. However, there are still several disadvantages in this method. Since it relies on the traditional stereo matching technique to find out the geometric information, it does not work with textureless and non-polygonal (viewpoint dependent) objects.

As sheet metal stamping workpieces are normally textureless and non-polygonal, stereo matching in visual images is non-feasible. In addition, since thermal images are vague and the texture resolution in thermal images is not as good as the texture (color) resolution in visual images, stereo matching between infrared thermal images fails to work as well. As silhouettes become the dominant feature over thermal images, we use octree carving technique [30] to acquire the

geometric information from the silhouettes of the object in thermal images. By using our method, 3D thermogram of sheet metal stamping workpieces can be acquired. With the same advantage of Nebel's method, we do not need to solve the template/texture fitting problem as the infrared camera is calibrated and the thermal signature information can be directly projected to the 3D model. Finally, our method minimizes the number of camera used. We only need one infrared camera while Nebel's method needs both visual cameras for geometric information and an infrared camera for thermal signature information. Since our method needs accurate calibration of infrared thermal cameras, net-and-board calibration scheme is also proposed to solve the technical problem.

3. Implementation of the Diagnosis System

In this chapter, it firstly describes the basic principles on thermograph acquisition. Then it shows the diagnosis system setup. Basically, it consists of an infrared camera, a tripod, a turntable and a net-and-board calibration box. After that, the perspective camera model is described. It is used to model the infrared camera in calibration and reconstruction. Next, it discusses how we calibrate our diagnosis system that involves an infrared camera. It introduces our proposed net-and-board calibration box for infrared camera calibration as traditional checkboard cannot be seen by infrared cameras. Finally, the reconstruction algorithm octree carving technique is discussed.

3.1 Thermograph acquisition

The most convenient method to obtain thermograph is using infrared cameras. The basic principle of infrared (IR) sensing has been well known nowadays. All objects with temperature over absolute zero degree emit electromagnetic energy called thermal radiation.

With thermal detectors whose signal is proportional to the absorbed energy, we can obtain the surface temperature without contacting with the object. The most common technique today is conventional passive radiation thermometry, but it must be used with caution to avoid systematic errors arisen from poorly

characterized target properties (emissivity, transmissivity) and extraneous background radiation. In our experiments, an infrared camera with sensitivity of 0.1°C is used and the model of the infrared camera is IR913 from manufacturer Guide. The resolution of the infrared camera is 308x226.

3.2 Diagnosis system setup

As the stamping process involved punching, it causes the workpiece deformation. The deformation hence makes the stress and strain distribution. By the conservation of energy, the stress and strain in the stamping object will transfer to the heat energy and causes thermal distribution. In our diagnosis system, what we need to do is to get the thermal distribution of the object after the stamping process immediately, as the heat will be lost due to surroundings. Since we need to reconstruct the object from several images, we need to take a sequence of images from different viewpoints. The experimental setup of our system basically consists of a stamping machine, a net-and-board calibration box, a tripod, an infrared camera and a turntable. Fig. 3.1 shows our system setup. Fig. 3.2 shows another closer shot of our system.

After calibrating the system and obtaining a sequence of infrared thermal images, we can use a computer to reconstruct the 3D thermal distribution by the reconstruction algorithm.

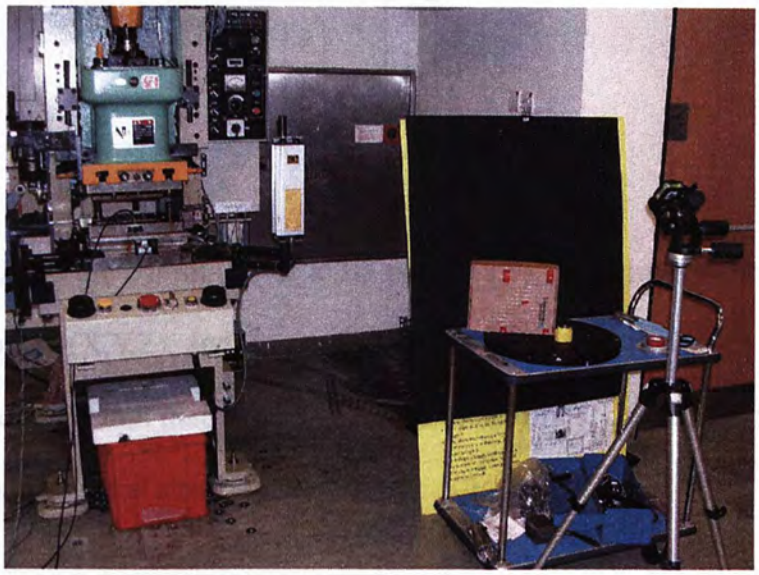

Fig.3.1 Experimental setup of our system

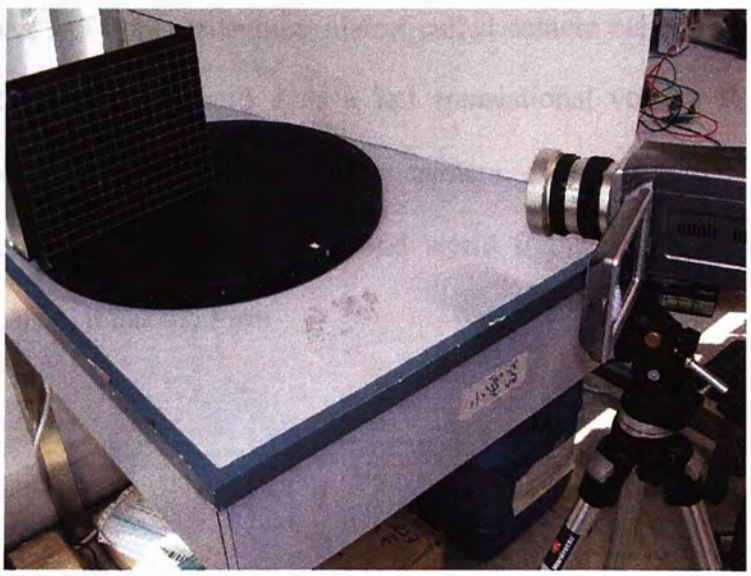

Fig.3.2 Another closer shot of our system

3.3 Perspective camera model

In computer vision, most of the cameras are modeled as a perspective camera. And, it can be expressed as follow

$$\omega \begin{bmatrix} u \\ v \\ 1 \end{bmatrix} = \mathbf{P} \begin{bmatrix} X \\ Y \\ Z \\ 1 \end{bmatrix} \tag{7}$$

where (X,Y,Z) is the coordinate of a 3D point, (u,v) is the image coordinates of the projection of (X,Y,Z), and ω is an arbitrary scale factor. $\mathbf{P}$ is a 3x4 matrix known as the projection matrix which models the pin-hole camera. The projection matrix $\mathbf{P}$ has a special structure given by

$$\mathbf{P} = \mathbf{K}[\mathbf{R} \mid \mathbf{t}] \tag{8}$$

where $\mathbf{K}$ is a 3x3 upper triangular matrix called camera calibration matrix, $\mathbf{R}$ is a 3x3 rotational matrix and $\mathbf{t}$ is a 3x1 translational vector. $\mathbf{R}$ and $\mathbf{t}$ are called the extrinsic parameters of the camera. They describe rigid body transformation between camera frame and world frame. And, $\mathbf{K}$ is a camera calibration matrix, it has the form

$$\mathbf{K} = \begin{bmatrix} af & \gamma & u_0 \\ 0 & f & v_0 \\ 0 & 0 & 1 \end{bmatrix} \tag{9}$$

where f is the focal length, a is the aspect ratio, and γ is the skew parameter, (u_0, v_0) is the principal point. They are all referred to the intrinsic parameters of the camera, and calibration is the process of estimating these parameters. Indeed, a camera is said to be calibrated if its intrinsic parameters are known. If both of the

intrinsic and extrinsic parameters are known, the camera is said to be fully calibrated.

3.4 System calibration

To reconstruct the model using octree carving technique, we have to know the intrinsic camera parameters and the camera orientations. To calibrate a camera system with its intrinsic and extrinsic parameters of the camera system, a chessboard can be used traditionally in visual images. Due to the even thermal distribution over the chessboard, however, the corner features of chessboard cannot be captured by an infrared camera [29]. Therefore, we can not use chessboard for infrared camera calibration. We propose two different calibration methods. One is the LEDs calibration board while the other one is the net-and-board calibration box. From the experiments, we found that the net-and-board calibration box is much more accurate and efficient than the LEDs calibration board. In the following subsections, we will discuss these two different methods.

3.4.1 LEDs calibration board

We put 6 x 6 LEDs on an electronic board and they are connected to power supply. After connecting with electricity, the LEDs light up and emit infrared rays. As a consequence, the LEDs can be viewed by an infrared camera. We tried to extract these LEDs positions in the infrared images for calibration. However, since the

diffusion of infrared light and the heat transfer from the LEDs to the electronic board. We can hardly extract the exact central points of the LEDs. Thus, it makes the calibration difficult and inaccurate. Fig. 3.3 shows infrared thermal images of the LEDs calibration board after connected to the electricity. Fig. 3.4 shows the corresponding extracted centre points of each LED. From these images, although we can extract the centre points, the extracted points deviate from their central points of the LEDs. Therefore, it makes the calibration inaccurate and difficult.

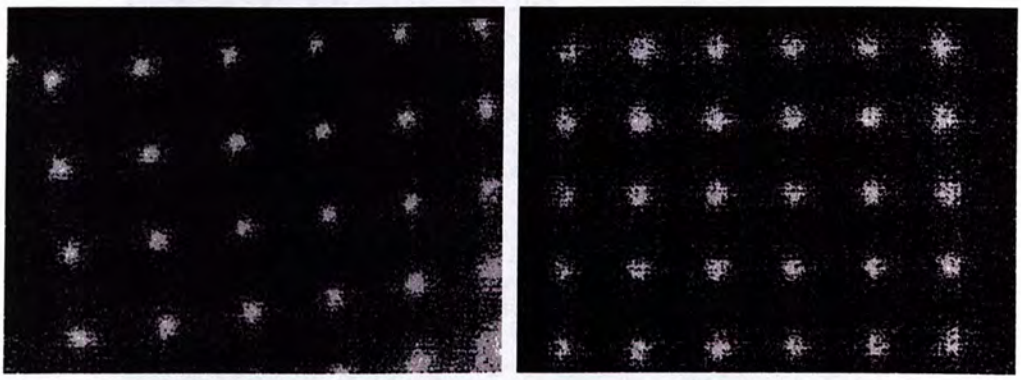

Fig.3.3 The infrared images of the LEDs calibration board

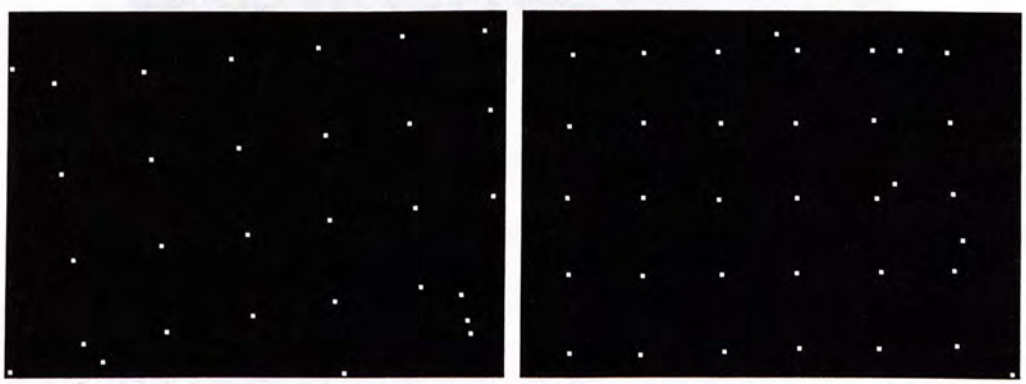

Fig.3.4 The corresponding extracted central points of each LED

3.4.2 Net-and-board calibration box

As LEDs calibration box fails to work well for infrared thermal camera calibration, we propose the net-and-board calibration box to calibrate the camera system. After extracting the corner information, we can calibrate the camera system using standard calibration algorithm [34]. The net is made of metals while the box is made of glass covered by a black plastic sheet, and it is shown in Fig. 3.5.

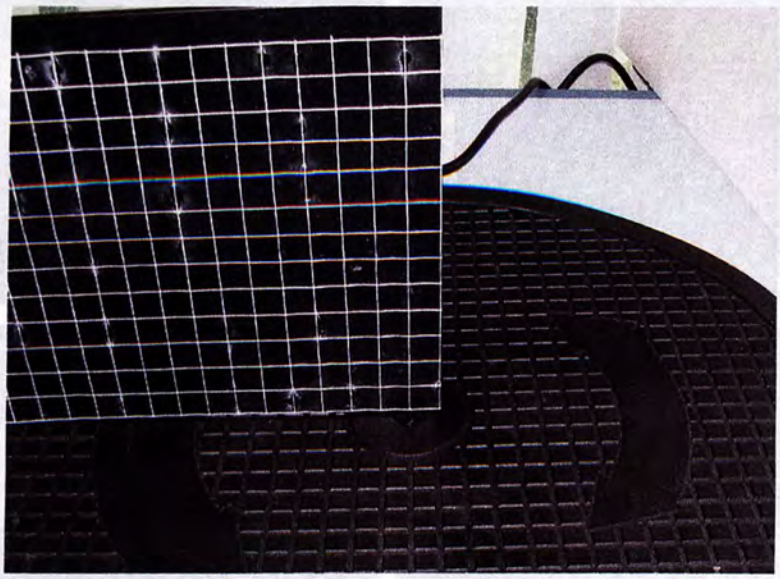

Fig.3.5 The net-and-board calibration box

As the net-and-board is made of different materials, it does provide distinct thermal features to the infrared camera when we blow the net-and-board box with hot air. It is because of the different rate of heat absorption for different materials.

The image sequence used for calibration and reconstruction are acquired by a fixed infrared camera and rotate on a turntable. The turntable is rotated by a fixed identical angle between each snap-shot. For our thermal reconstruction model, the

rotation angle between two successive images is 20 deg and the whole sequence consists of eighteen images. It means that the turntable is rotated 360 deg (one revolution). At the beginning, we take 4 images (308x226) of the net-and-board calibration box at 20 deg intervals. These 4 calibration images captured by an infrared camera are shown in Fig. 3.6.

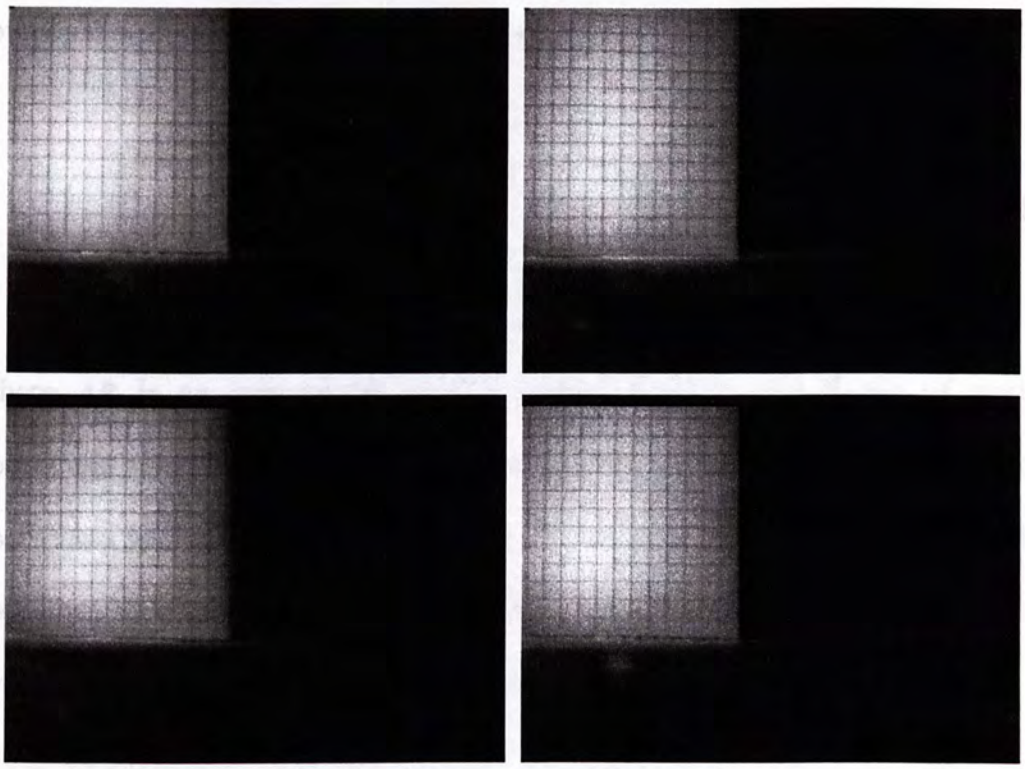

Fig.3.6 The infrared images of the net-and-board calibration box

The projection matrix P_1 for the first camera is then decomposed into the camera calibration matrix K, the rotation matrix R and the translation vector t as follows

$$P_1 = K[R \quad t] \tag{10}$$

Since it is not always possible to see the front face of the net-and-board calibration box when performing a complete rotation on a turntable, some of the views can not be calibrated directly from the corresponding images of the net-and-board calibration box as the camera is facing the back of the box. Thus, these views are calibrated by multiplying rotational matrices.

To obtain the remaining projection matrices for all the views, we multiply the rotation matrix $\boldsymbol{R}$ by an incremental rotation matrix $\Delta\boldsymbol{R}$ as follows

$$\Delta\boldsymbol{R} = \begin{pmatrix} \cos\theta & 0 & -\sin\theta \\ 0 & 1 & 0 \\ \sin\theta & 0 & \cos\theta \end{pmatrix} \tag{11}$$

where $\Delta\boldsymbol{R}$ is an incremental rotation matrix, $\theta = 20^\circ$, the Y-axis of world coordinate coincides with the rotational axis of the turntable, the X-axis of world coordinate is located horizontally on the front face, and the Z-axis of world coordinate is pointed outward from the front face. Thus, the projection matrices for all the cameras cab then be generated by

$$\boldsymbol{P}_i = \boldsymbol{K}\left[\boldsymbol{R} * \Delta\boldsymbol{R}^{i-1} \quad \boldsymbol{t}\right] \tag{12}$$

where i=1 to 18 for our thermal reconstruction model.

After the calibration of camera system, the x-axis (horizontal) and y-axis (vertical) image plane of reprojection error is [0.17714 0.17549] in unit pixel, respectively. The origin is located at the top-left corner of the image plane. The

error is quite small, and thus demonstrates the effectiveness and practicality of our proposed net-and-board calibration box for infrared camera system calibration. Fig. 3.7 shows the reprojection of the four infrared images of the net-and-board calibration box.

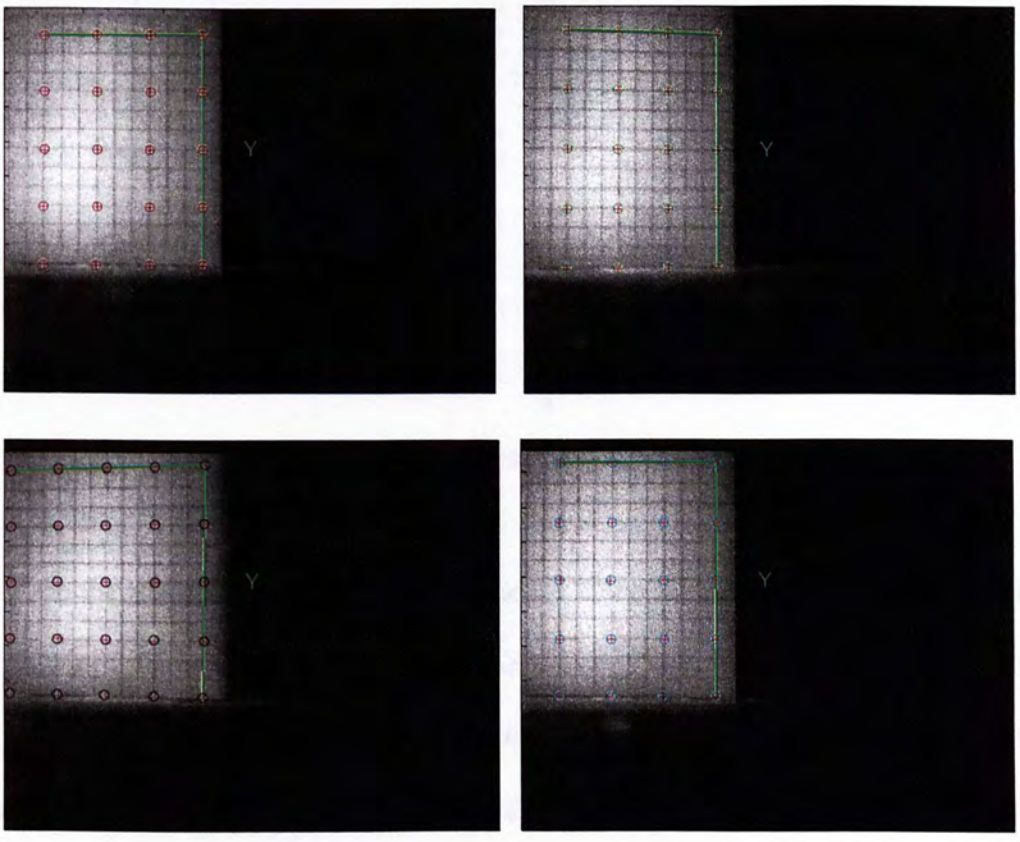

Fig.3.7 Reprojection images of the net-and-board calibration box
(image points + and reprojection points o)

Fig. 3.8 shows the reprojection error diagram of the four calibration images.

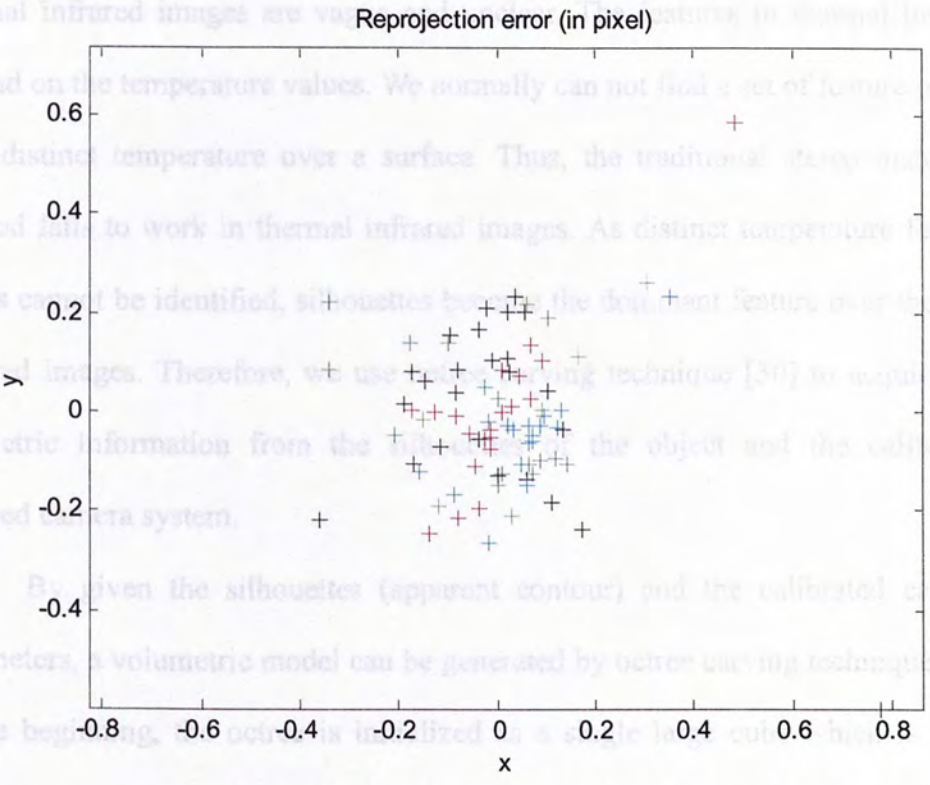

Fig.3.8 Reprojection error diagram of the images

In the robotic arm experiment in chapter 7, we fill the net-and-calibration box with water. Since specific heat capacity of water is high and the black plastic sheet cover is directly attached to the box, it helps further separate the specific heat capacity of the black plastic cover and the net. Therefore, the net pattern can be seen from the infrared camera much more easily.

3.5 Reconstruction algorithm

Traditionally, we have to find out the correspondences between images to get the 3D geometric information. However, unlike visual images, the feature points in

thermal infrared images are vague and unclear. The features in thermal images depend on the temperature values. We normally can not find a set of feature points with distinct temperature over a surface. Thus, the traditional stereo matching method fails to work in thermal infrared images. As distinct temperature feature points cannot be identified, silhouettes become the dominant feature over thermal infrared images. Therefore, we use octree carving technique [30] to acquire the geometric information from the silhouettes of the object and the calibrated infrared camera system.

By given the silhouettes (apparent contour) and the calibrated camera parameters, a volumetric model can be generated by octree carving technique [30]. In the beginning, the octree is initialized as a single large cube which is large enough to enclose the reconstructed model. Then the root cube is projected onto the images and classified as either (1) completely outside the apparent contour, (2) completely inside the apparent contour, or (3) ambiguous (partially inside the contour). If the cube is classified as (3), it is subdivided into 8 sub-cubes, and each of them is projected onto the images and classified again. This process is repeated until a predefined maximum level is reached. If the cube is classified as (1), it is thrown away. Only category (2) and (3) are used to constitute the volumetric model of the object. Fig. 3.9 shows the volumetric representation of the octree classification. And the algorithm of octree carving technique [30] is summarized in Fig. 3.10.

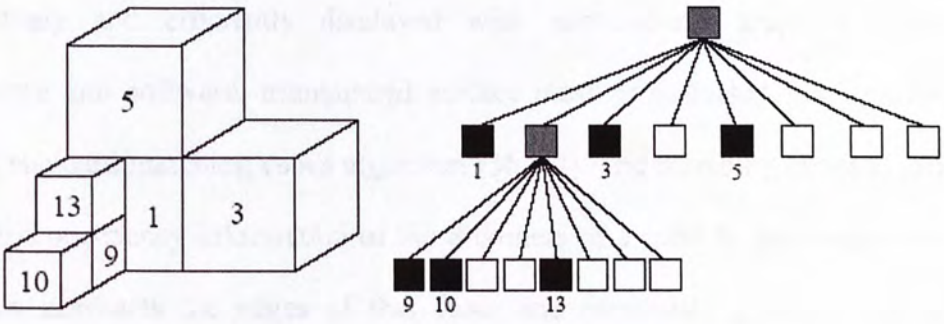

Fig.3.9 Volume representation of octree
and the corresponding tree structure. [35]
White cube is the cube in category (1).
Black cube is the cube in category (2).
Gray cube is the cube in category (3).

Octree carving technique

Initialize a cube that enclose the whole model
While max level not reached **do**
    For each cube in the current level **do**
        Project the cube onto each image and classify either as follows:
            (1) Completely outside the apparent contour
            (2) Completely inside the apparent contour
            (3) Ambiguous
        if the cube is classified as category (3) **then**
            subdivide the cube into 8 sub-cubes
            add the sub-cube to the next level
        end if
    end for
    increase the level count
end while

Fig.3.10 Algorithm of octree carving technique

In order to make the reconstructed 3D thermal distribution model to be effectively and efficiently displayed with conventional graphics rendering hardware and software, triangulated surface mesh is extracted from the octree using standard marching cubes algorithm [36, 37]. The marching cubes algorithm uses the occupancy information of the 8 corners of a cube to determine how the surface intersects the edges of that cube, and eventually generates triangular patches which best approximate the surface. For the thermal information of the object, we use coloring of vertex instead of texture mapping. By using coloring of vertex, it gives a smooth thermal signature rather than discrete and fragmentary. The color of each vertex in the mesh is estimated. The estimated color is basically a weighted average of all the pixel color of the projections of that vertex. The weighting factor for each image is the cosine of the angle (dot-product) between the viewing direction and the surface normal at that vertex [35]. The weighting factor is as follows

$$\omega_i = \begin{cases} -\mathbf{n} \cdot \mathbf{v}_i & \text{(if visible)} \\ 0 & \text{(otherwise)} \end{cases} \tag{13}$$

where $\boldsymbol{n}$ is the unit normal vector of the vertex (pointing outward) and $\boldsymbol{v}_i$ is the unit viewing direction vector of view i.

3.6 Summary

In this chapter, the basic principles on thermograph acquisition are described. Then it shows the diagnosis system setup. After that, the perspective camera model is described. It is used to model the infrared camera in calibration and reconstruction. Next, it discusses how we calibrate our diagnosis system that involves an infrared camera. It introduces our proposed net-and-board calibration box for infrared camera calibration as traditional checkboard cannot be seen by infrared cameras. Finally, the reconstruction algorithm octree carving technique is discussed.

4. Consistency from Different Viewpoints

In this section, we will describe the experiment setup to make sure that the system is in an omni-directional infrared environment. When we reconstruct a 3D model from optical images, the color at a certain point of the object captured by a camera may be different from different viewpoints. It is normally due to the light reflection and it can be solved using weight average of all the pixel color of the projections of that vertex. It can also be solved by omni-directional lighting environment. In our experiment, we have to make sure the experiment setup is in an omni-directional infrared environment (i.e. there is no additional heat source that is affecting the thermal images captured by the infrared camera) before a sequence of thermal images of the workpiece is captured for 3D thermal distribution reconstruction. Therefore, we have to conduct an experiment to verify the consistency of thermal values captured by an infrared camera from different viewpoints. It is also used to show that the experiment is in an omni-directional infrared environment.

In our experiment, it consists of a "validation resistor-box", a turntable, a laser thermometer, and an infrared camera. Fig. 4.1 shows the "validation resistor-box".

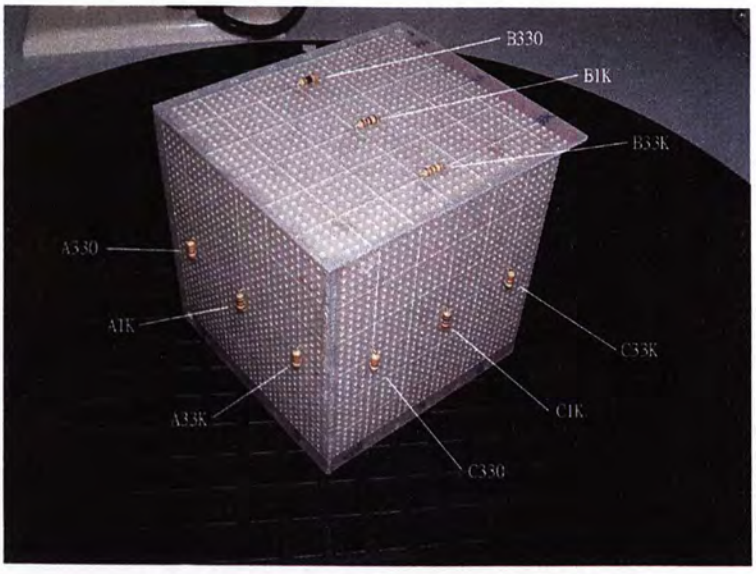

Fig.4.1 The validation resistor-box

Basically, this box consists of three faces, and they are named as face A, B and C. In each face, there are three different resistors: 330Ω, 1KΩ and 33KΩ. At each face, the three resistors are connected in parallel to a 6V DC supply. By the power law, the smaller the resistance of the resistor, the higher the power that it consumes, and thus it would be the hottest resistor among the three and vice versa. After connecting to the power supply, the temperatures of the resistors start to rise over time. Fig. 4.2 shows the temperatures of the resistors measured by a laser thermometer over time. We firstly measure the temperatures before turning on the supply. Next, we measure the temperatures at one minute interval after turned on for three minutes.

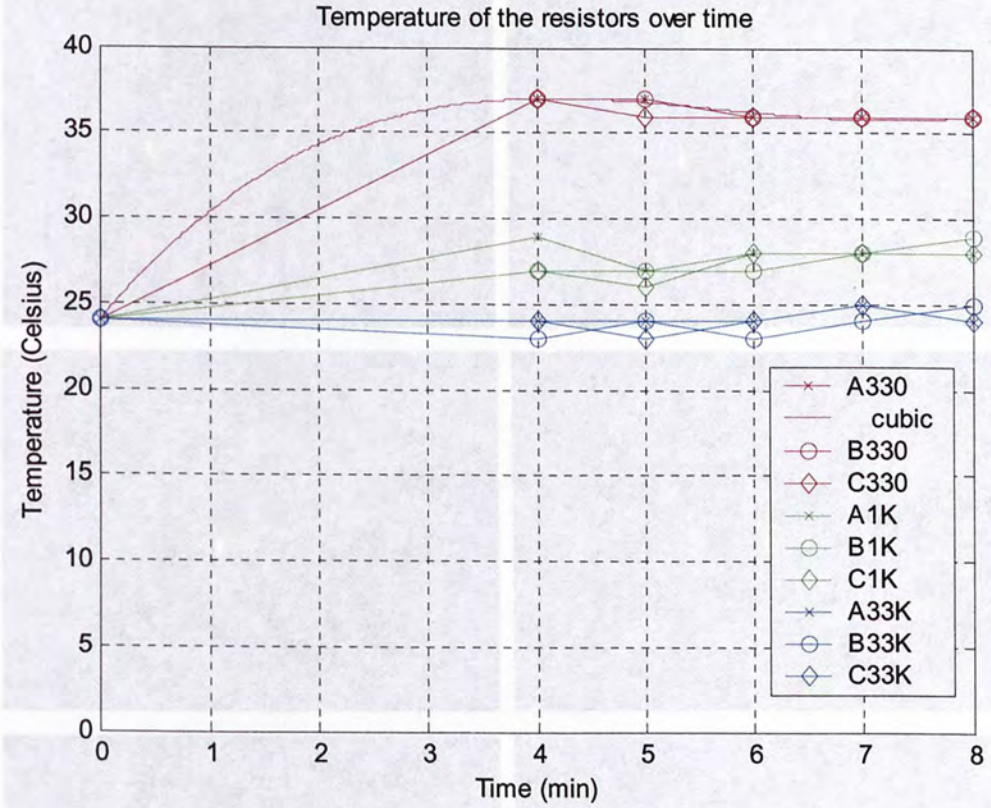

Fig.4.2 Temperatures of the resistors over time

In Fig. 4.2, the cubic curve fits the values of the 330Ω resistors so as to give the general temperature information between time 0 min and time 4 min. After 7 min, the temperatures of all the resistors become steady, and we can take thermal infrared images of the box from different viewpoints to verify the measured results. Fig. 4.3 shows a sequence of the thermal infrared images for this "validation resistor-box" and its corresponding temperature color palette. All the images are taken at 20 degrees intervals.

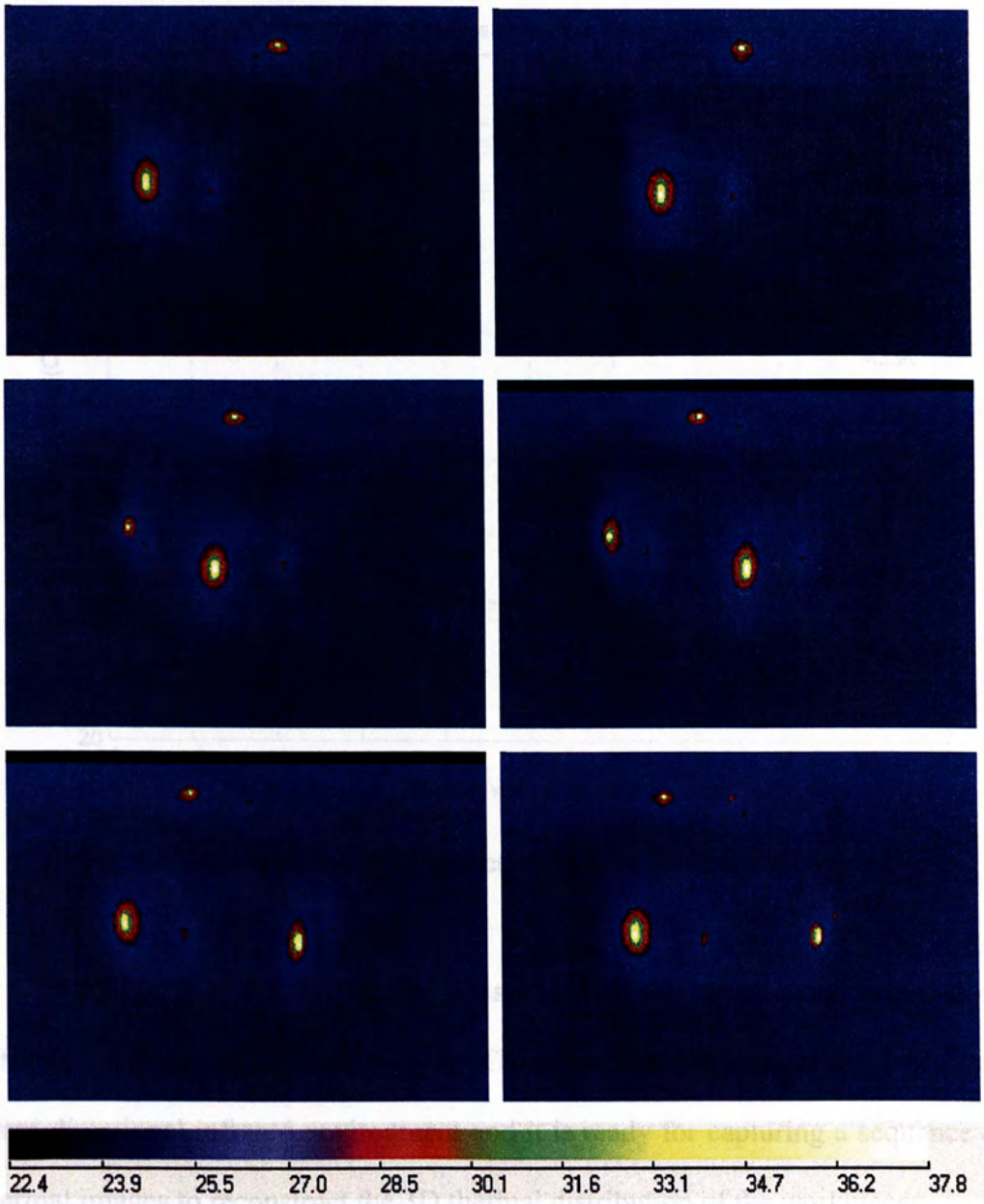

Fig.4.3 The thermal images sequence of the box

After capturing the images sequence, we can obtain the temperatures of all the resistors from the infrared camera software. Fig. 4.4 shows the temperatures of all the resistors from different viewpoints using the thermal images.

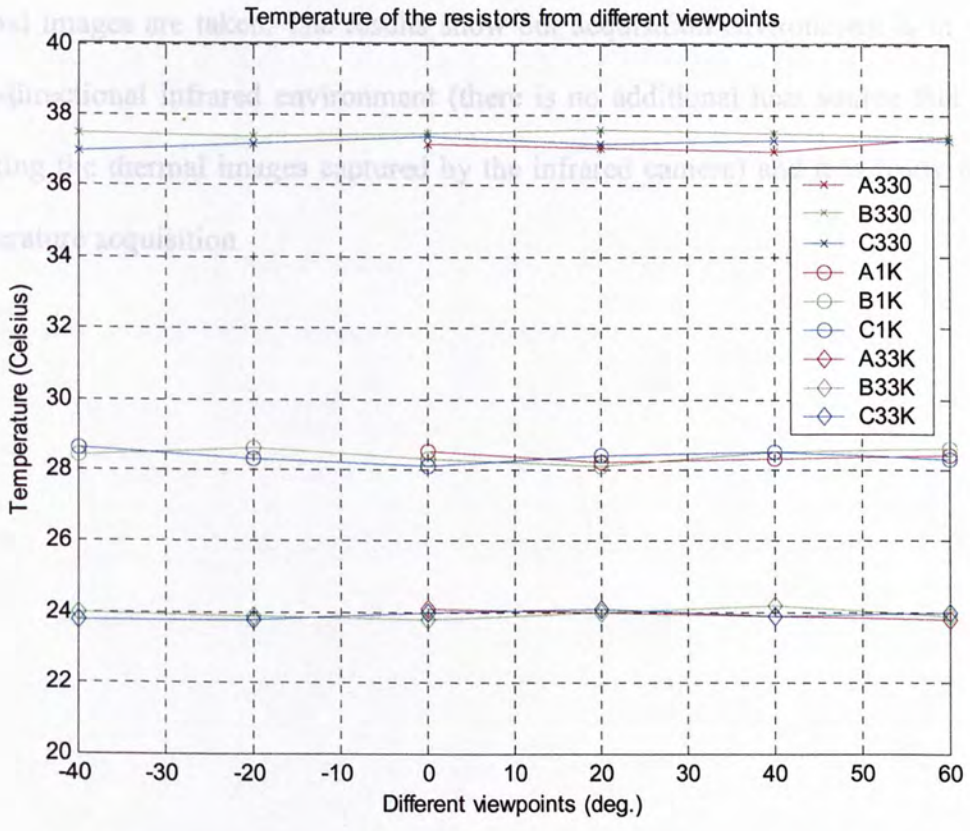

Fig.4.4 Temperatures of all the resistors from different viewpoints

From Fig. 4.4, we can see the consistency of the temperature values from different viewpoints for each resistor. Therefore, the experiment setup is in an omni-directional infrared environment and it is ready for capturing a sequence of thermal images to reconstruct the 3D thermal distribution of the workpieces.

4.1 Summary

This chapter describes the experimental setup for ensuring the acquisition environment where consistency of temperature from different viewpoints is achieved. Basically, a validation resistor box is made. Then a set of infrared

thermal images are taken. The results show our acquisition environment is in an omni-directional infrared environment (there is no additional heat source that is affecting the thermal images captured by the infrared camera) and it is ready for temperature acquisition

5. Visual Reconstruction of Objects

In this chapter, visual images are used to reconstruct visual models based on the reconstruction algorithm "octree carving technique" described in chapter 3. A digital visual camera is used in the experiments. In these experiments, the visual reconstruction models are used for realistic perceptions. A "Siu Sun" cartoon model and a stamping disc are used as examples for illustration.

For smooth textureless surfaces, especially in stamping workpieces, we do not have any cues to find the correspondences as it has no corners and surface markings. Thus, we cannot use the traditional method to find the corresponding points and reconstruct the 3D models. In smooth textureless surfaces, the dominant image feature is the silhouette (i.e. appararent contour, occluding contour, profile or outline). Silhouette is the projection of the locus of points on the surface at which the line of sight is orthogonal to the surface normal. In contrast to the features arising from corners, edges and surface markings, which are viewpoint independent, silhouettes is inherently viewpoint dependent. For example, two silhouettes of an arbitrary smooth object observed from two distinct viewpoints are the projections of two distinct curves in space. Thus, they do not provide correspondences, and we therefore use the octree carving method [30] to reconstruct the model instead of stereo matching methods. The two results show the successful reconstruction in visual images using octree carving method.

5.1 Visual camera calibration

To reconstruct a model from silhouettes, we need to calibrate both the intrinsic and extrinsic parameters of the camera system. Since we use visual images this time, we put a checkboard on the turntable to calibrate the extrinsic camera parameters and the intrinsic camera parameters of the camera. In this calibration, we use standard calibration method [13] and the method described in chapter 3.4 to fully calibrate the camera system. Fig. 5.1 shows four of the calibration images.

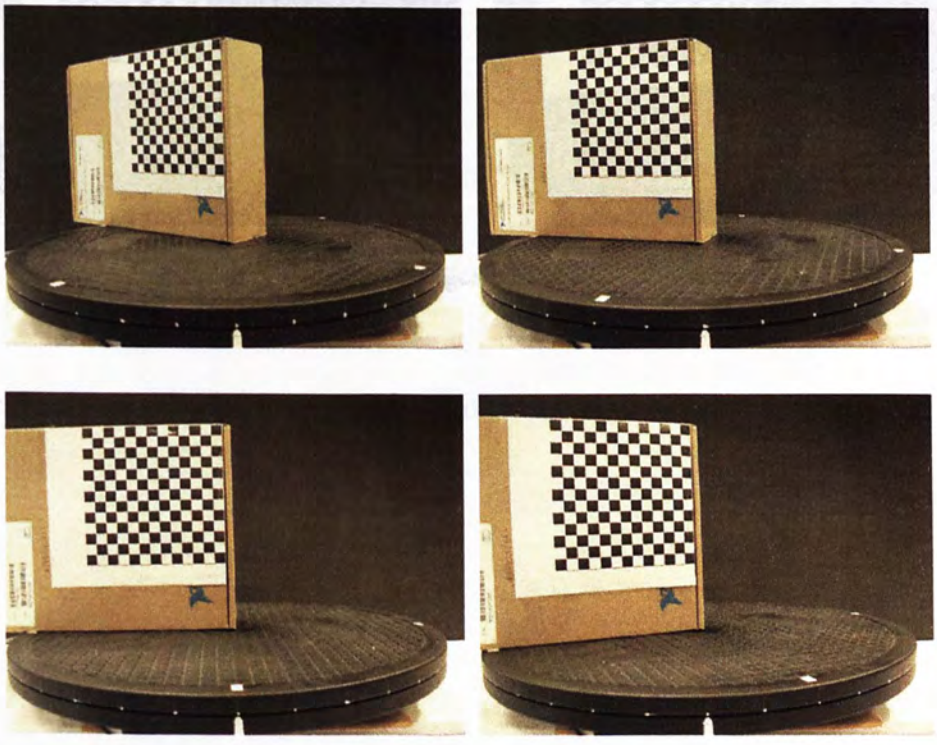

Fig.5.1 Four of the calibration images

Fig. 5.2 shows the reprojected corners of the corresponding images.

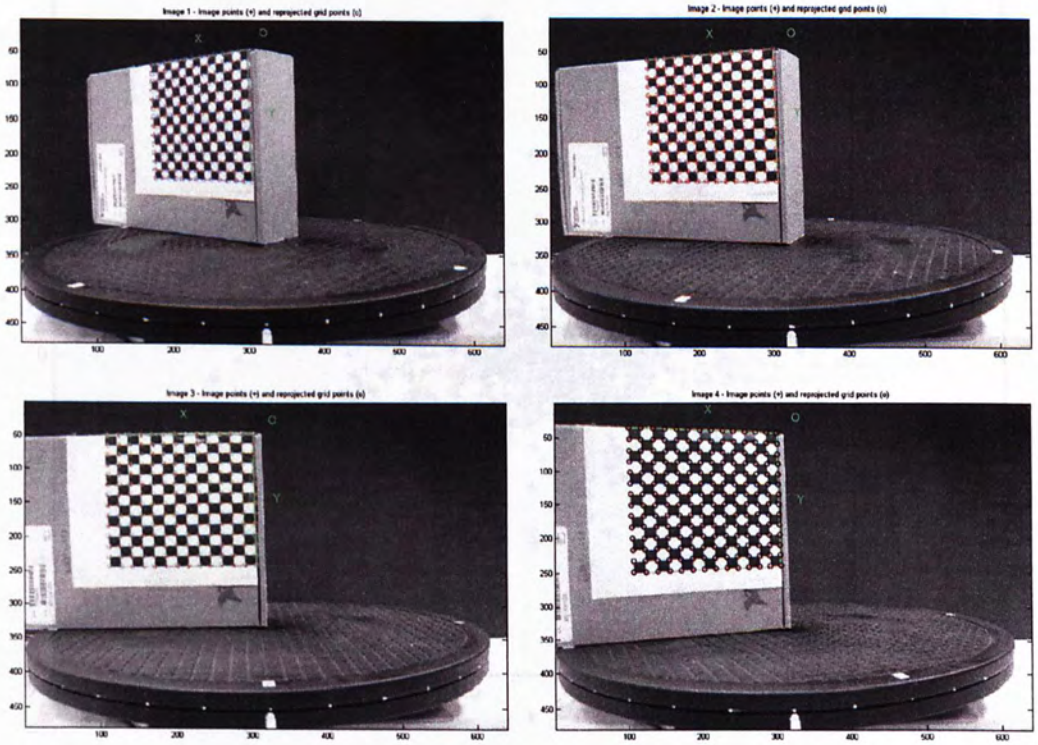

Fig.5.2 Reprojected images of the turntable sequence

After that, Fig. 5.3 shows the reprojection error diagram of the images.

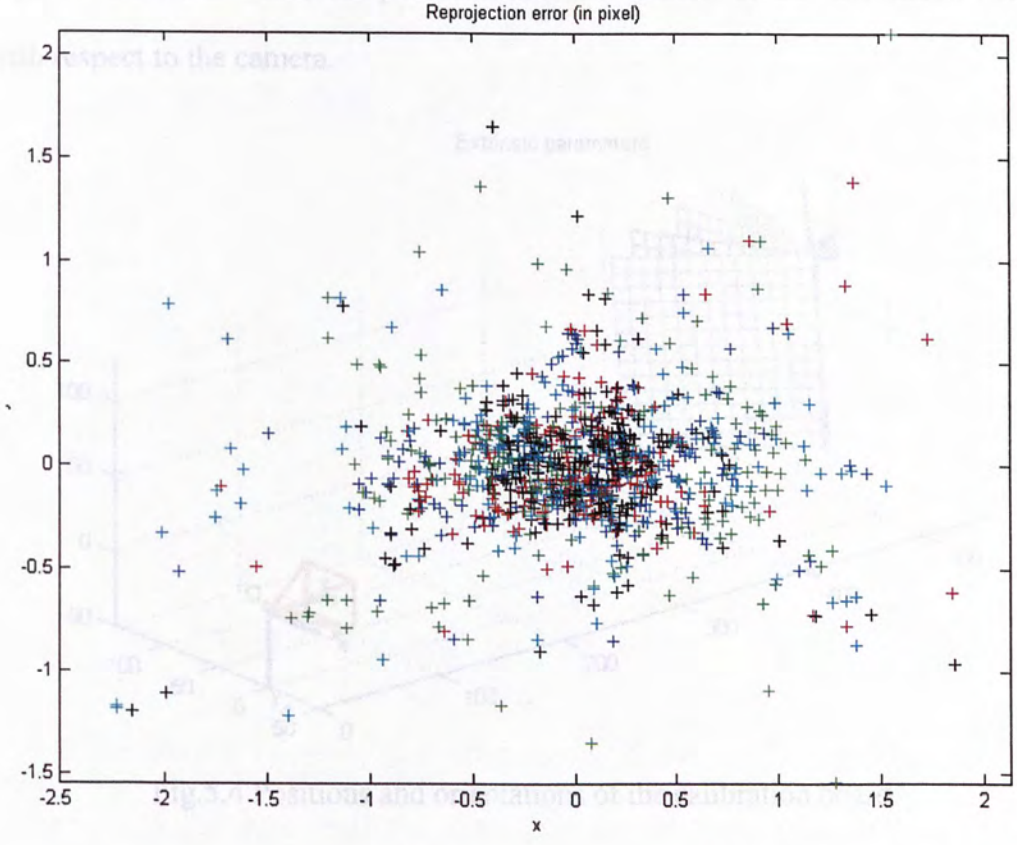

Fig.5.3 Reprojection error diagram of the images

The average reprojection error is [0.56491 0.33921] for x-direction and y-direction, respectively.

Fig. 5.4 shows the different positions and orientations of the calibration board with respect to the camera.

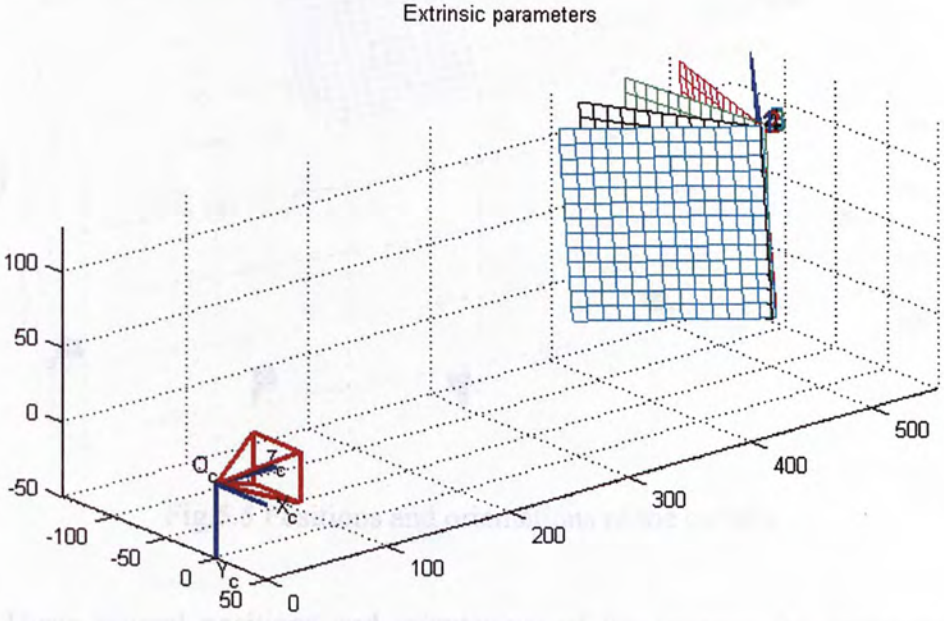

Fig.5.4 Positions and orientations of the calibration board

Fig. 5.5 shows the different positions and orientations of the camera with respect to the calibration board.

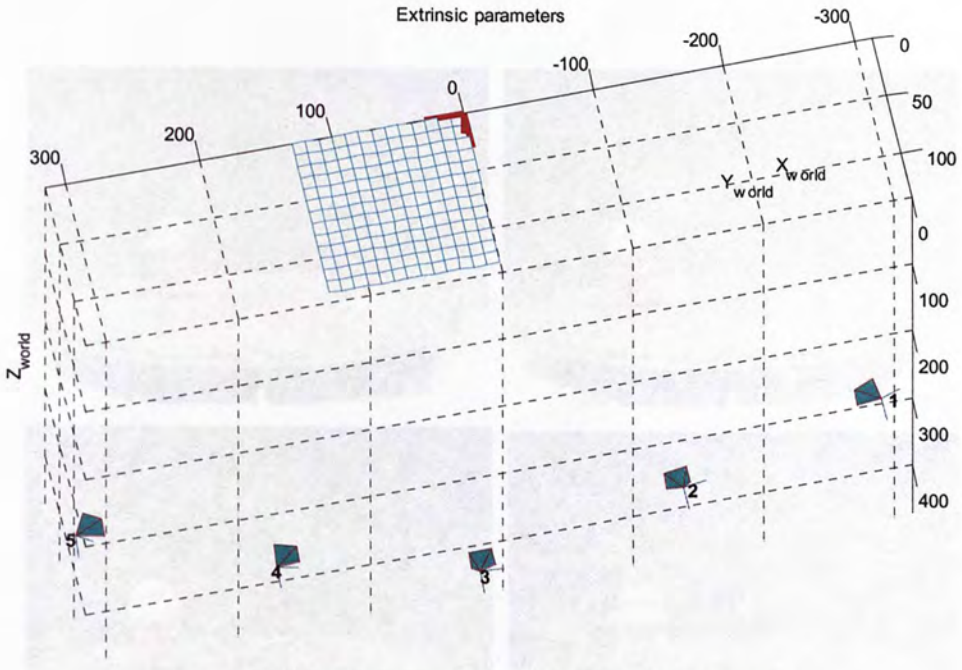

Fig.5.5 Positions and orientations of the camera

These several positions and orientations of the cameras (or relatively the calibration board) are calibrated directly from the checkerboard. However, since it is impossible to see the front face of the checkerboard after rotating 180 deg, the remaining positions and orientations of the cameras are calculated by (11) and (12) in section 3.4.2.

5.2 Results

5.2.1 Cartoon model "SiuSun"

We use a cartoon model "SiuSun" for the reconstruction. It demonstrates the fineness of the reconstructed model. Fig. 5.6 shows six out of 18 images for performing the reconstruction.

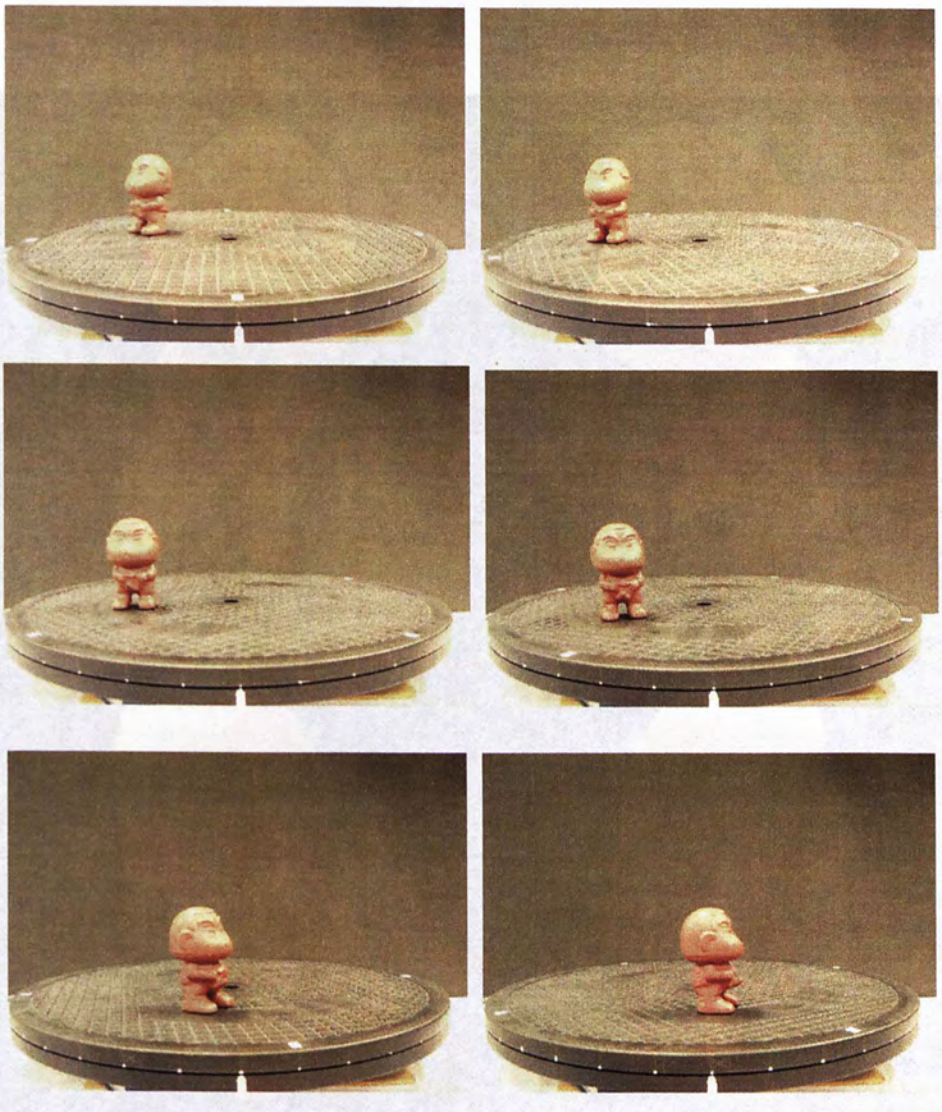

Fig.5.6 Image sequence of "SiuSun" model

The reconstructed result is shown in Fig. 5.7

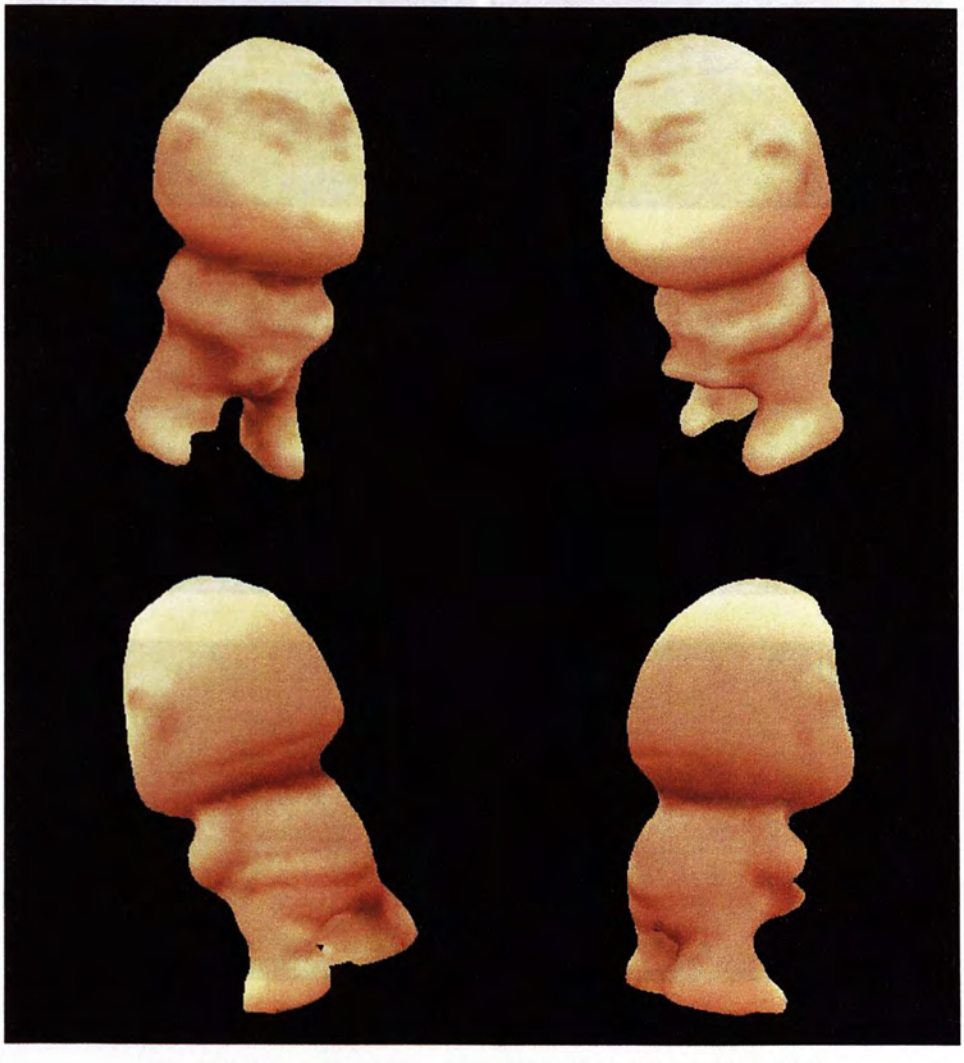

Fig.5.7 Reconstruction result of the "SiuSun" model

5.2.2 Stamping disc

We also use a stamping disc for the reconstruction. Fig. 5.8 shows six out of 36 images for performing the reconstruction. The first three are taken from the horizontal direction, and the last three are taken from the 45 degree inclination.

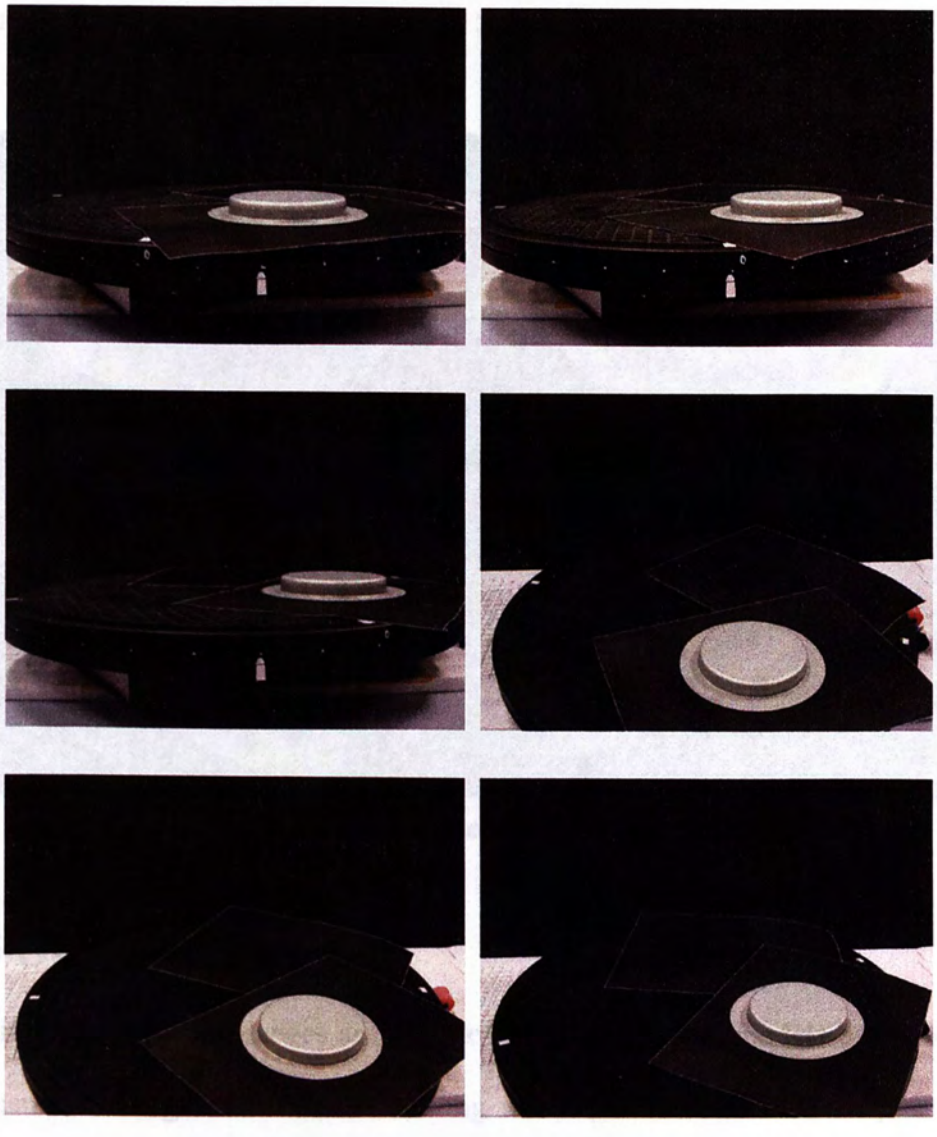

Fig.5.8 Six out of 36 images of the stamping disc

The reconstructed result is shown in Fig. 5.9

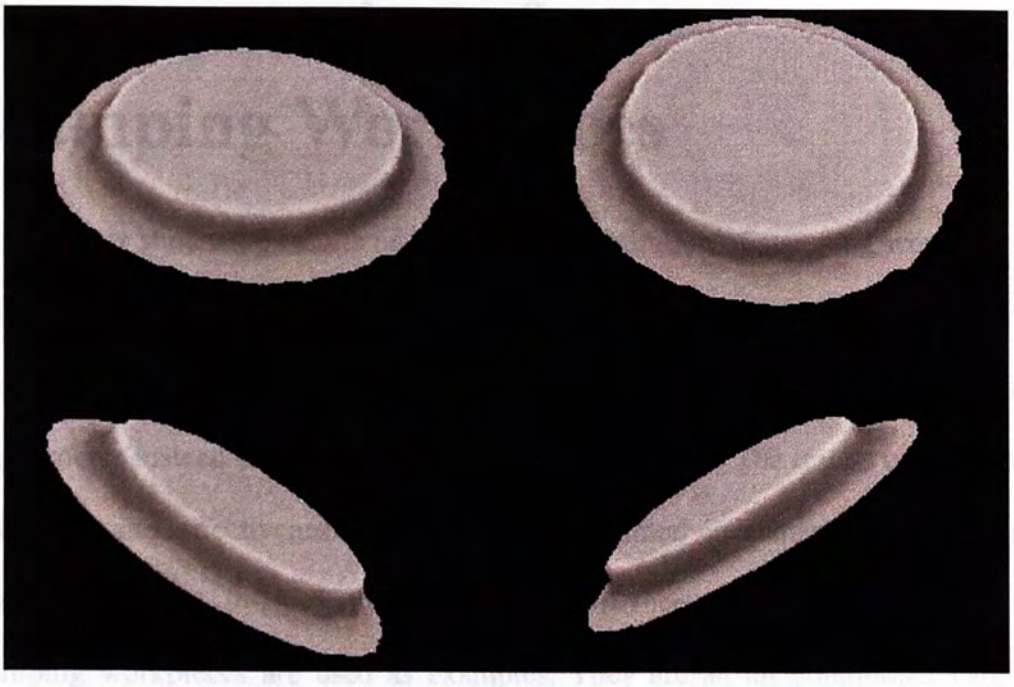

Fig.5.9 Reconstruction result of the stamping disc

5.3 Summary

In this chapter, visual images are used to reconstruct visual models based on the reconstruction algorithm "octree carving technique" described in chapter 3. A digital visual camera is used in the experiments. In these experiments, the visual reconstruction models are used for realistic perceptions. A "Siu Sun" cartoon model and a stamping disc are used as examples for illustration.

6. Thermal Distribution Reconstruction of Stamping Workpieces

This chapter shows the results of 3D thermal distribution of stamping workpieces from infrared thermal images solely. The reconstruction algorithm is the one described in chapter 3. A digital infrared thermal camera is used in these experiments instead of a digital visual camera in chapter 5. The results confirm the feasibility and effectiveness of our proposed method in acquiring 3D thermal distribution from infrared thermal images of sheet metal stamping. Three stamping workpieces are used as examples. They are an air conditioner cap, a deep drawing cup and a stamping cylinder.

6.1 Infrared camera calibration

To reconstruct the shape objects from its infrared images, we have to calibrate the infrared camera system. In this calibration process, we cannot use a checkerboard to perform camera calibration, it is due to the even temperature distribution on the checkerboard. Therefore, we use the net-and-board calibration box described in section 3.4 to calibrate the infrared camera system.

Firstly, we use a hair dryer to blow the net-and-board calibration box with hot air. As the material of the net is different from the material of the plastic sheet

cover, there is a temperature difference because of the different rate of heat absorption for different materials. Thus, we can clearly see the grid pattern in the infrared camera. After the calibration process, the positions and orientations of the calibration box with respect to the camera is shown in Fig. 6.1.

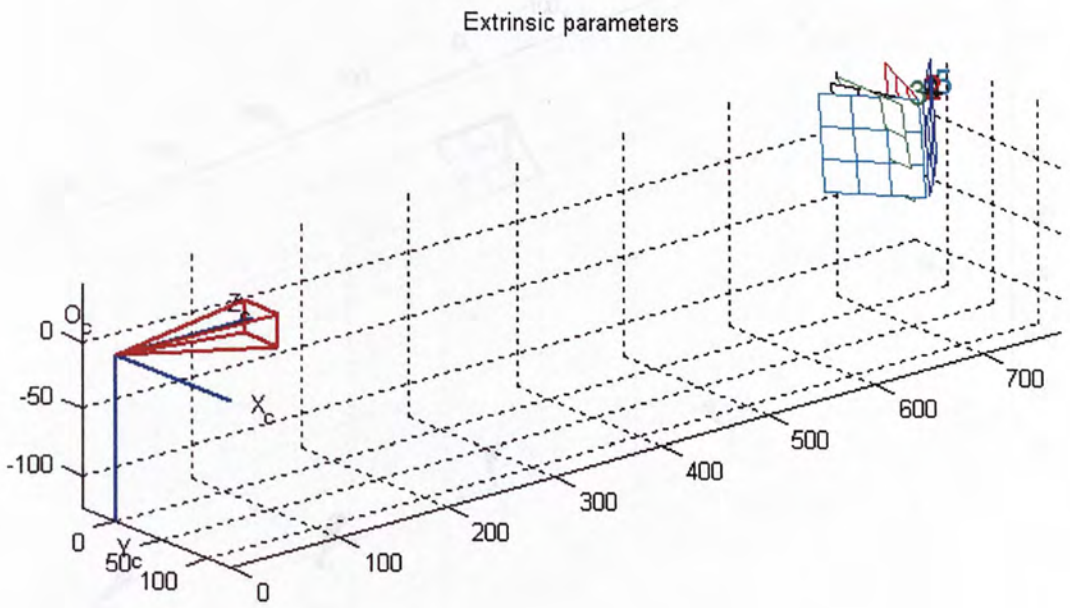

Fig.6.1 Positions and orientations of the calibration box

The positions and orientations of the infrared camera with respect to the calibration box is shown in Fig. 6.2.

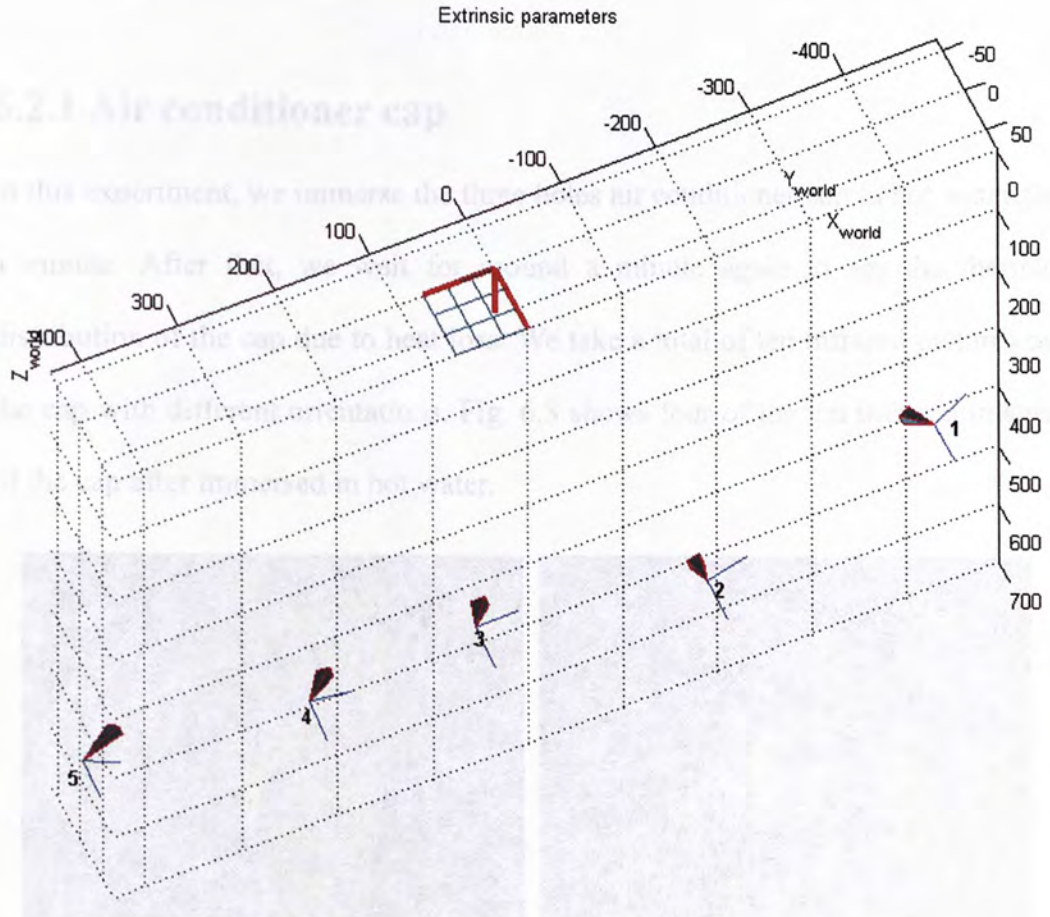

Fig.6.2 Positions and orientations of the infrared camera

Since it is impossible to directly calibrate all the positions and orientations, the remaining positions and orientations of the infrared camera are calculated by matrix multiplication in section 3.4.

6.2 Results

We have reconstructed the thermal distribution of an air conditioner cap, a deep drawing cup and a stamping cylinder in KS factory.

6.2.1 Air conditioner cap

In this experiment, we immerse the three holes air conditioner cap in hot water for a minute. After that, we wait for around a minute again to see the thermal distribution of the cap due to heat loss. We take a total of ten infrared pictures on the cap with different orientations. Fig. 6.3 shows four of the ten infrared images of the cap after immersed in hot water.

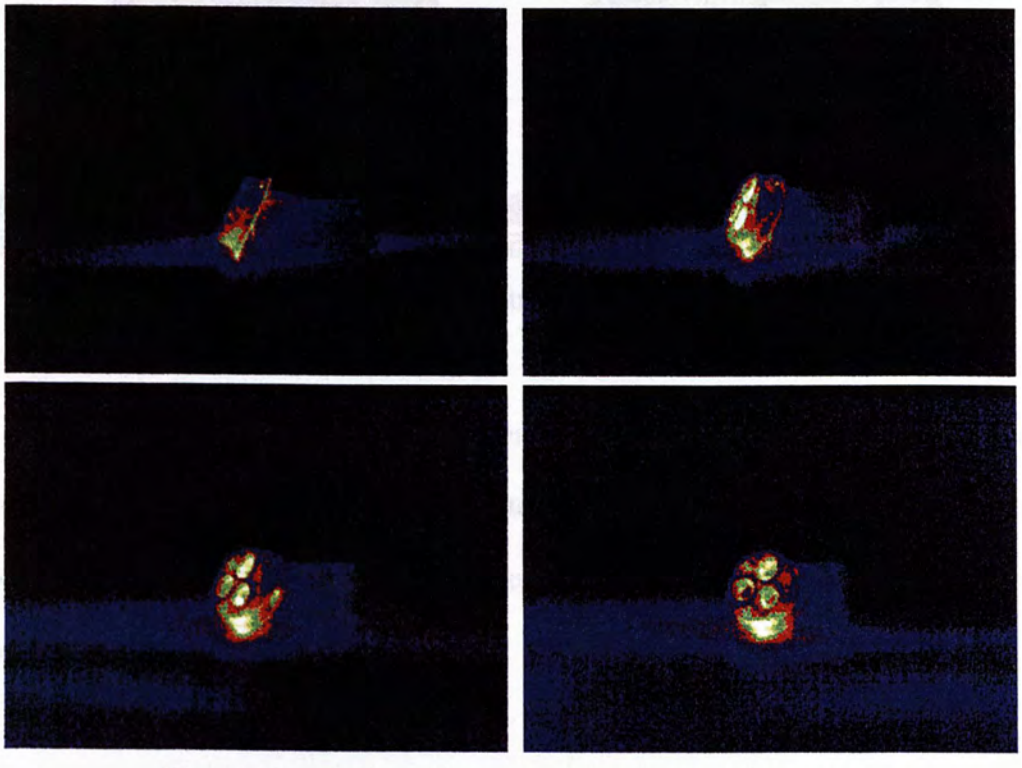

Fig.6.3 Four infrared images of the air conditioner cap

The reconstruction result is shown in Fig. 6.4.

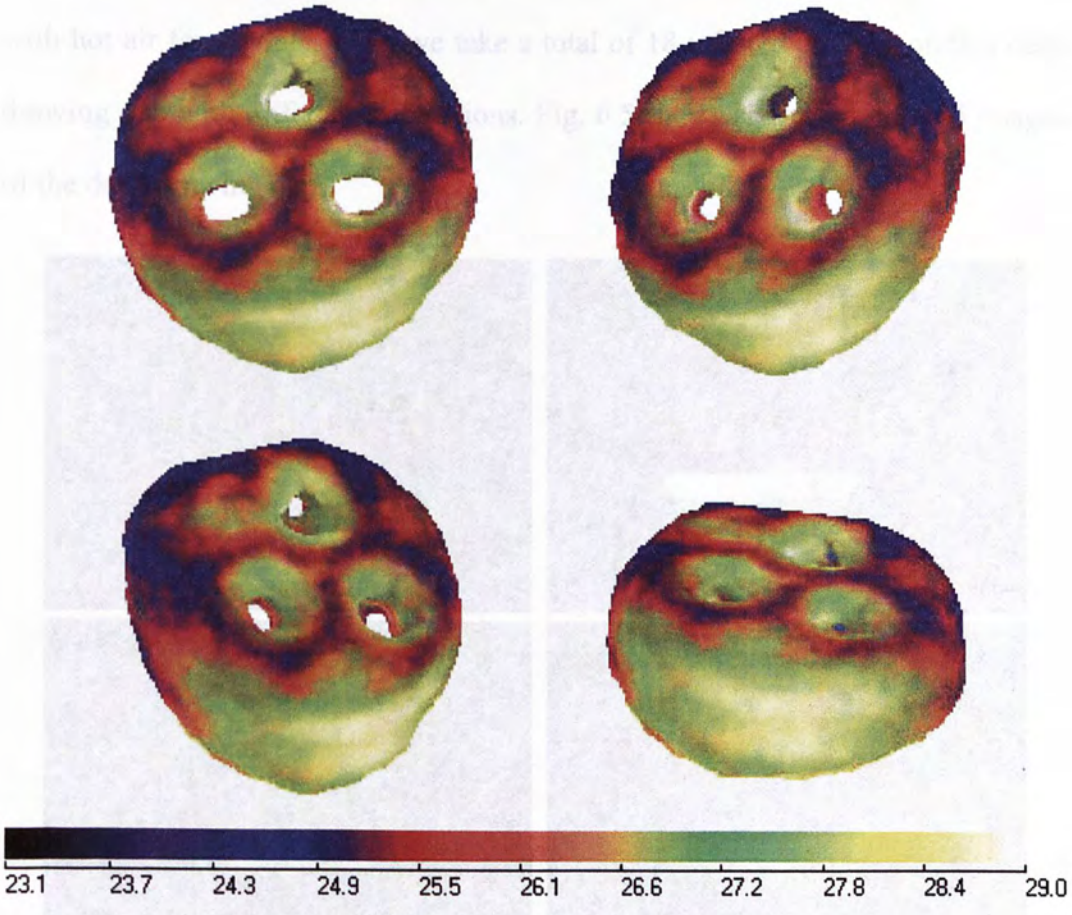

Fig.6.4 Thermal reconstruction result of the cap

From the above reconstruction result, we can clearly see the reconstructed model of the air conditioner cap. The rate of heat loss varies from place to place. Normally, it varies from geometric shape of an object, material, environment and etc.

6.2.2 Deep drawing cup

In this experiment, we blow the most deformed region of the deep drawing cup with hot air for a while. Then we take a total of 18 infrared pictures on this deep drawing cup with different orientations. Fig. 6.5 shows six of the infrared images of the deep drawing cup.

Fig.6.5 Six infrared images of the cup

The reconstruction result is shown in Fig. 6.6.

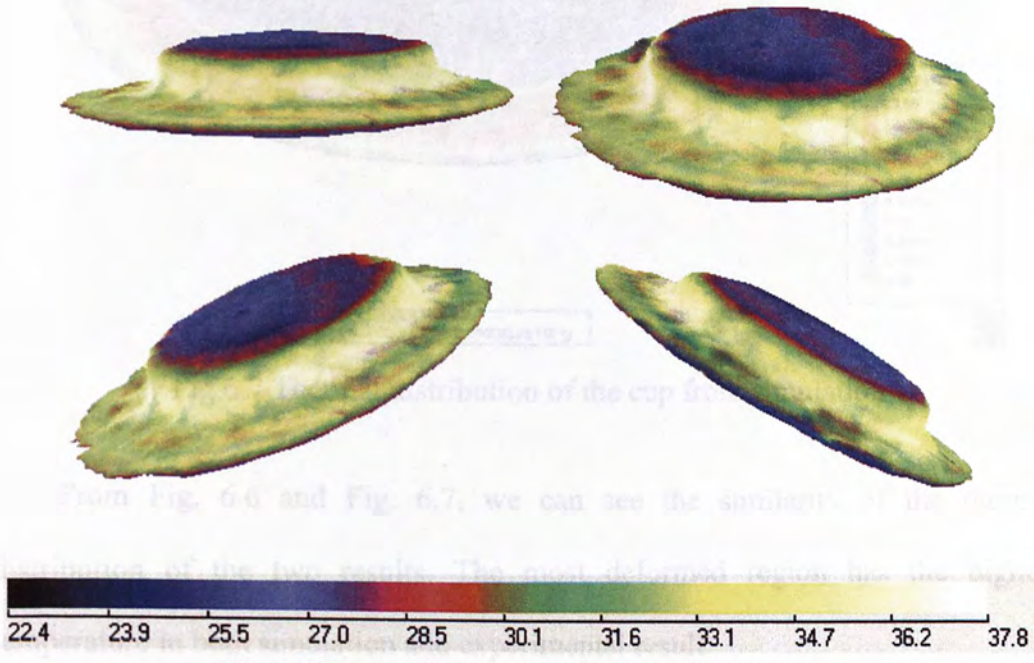

Fig.6.6 Thermal reconstruction result of the cup

From the above reconstruction result, we can see the thermal distribution of the deep drawing cup from the hottest region to the coldest region. We did a simulation on thermal distribution of the deep drawing cup in similar stamping operation by FEA. Fig. 6.7 shows the simulation result of the cup.

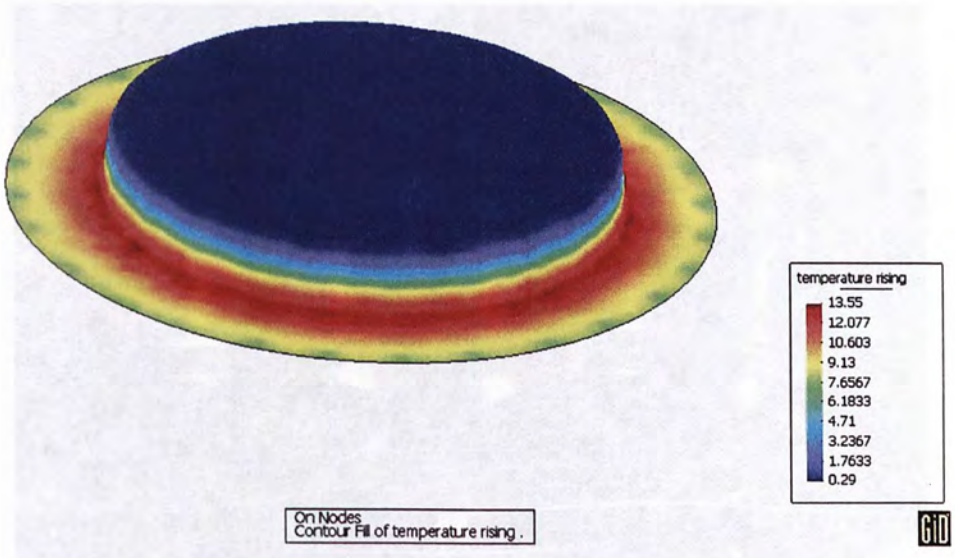

Fig.6.7 Thermal distribution of the cup from simulation

From Fig. 6.6 and Fig. 6.7, we can see the similarity of the thermal distribution of the two results. The most deformed region has the highest temperature in both simulation and experimental result.

6.2.3 Stamping cylinder from KS Factory

This experiment was conducted in King Siu Metal Factory in Shenzhen, China. The stamping cylinder we investigate is shown in Fig. 6.8. Clearly, it consists of five steps from a sheet metal blank to the final product. After each step, the intermediate workpieces are placed in a basket and waiting for the next step of stamping operation. Therefore, please be noted that this is an ordinary multi-steps stamping operation but not a progressive stamping operation.

Fig.6.8 The stamping cylinder from KS Factory

From Fig. 6.8, the sheet metal blank is at the bottom. The intermediate workpieces are at the top except that the final product is at the top right corner. Since the intermediate workpieces are placed in baskets and waiting for the next step of stamping operation, the heat generated from the previous step of stamping operation has totally lost to the surroundings already. As a consequence, we can consider that the heat generated is entirely from the current step of stamping operation. Therefore, it does not matter whether you choose any one of the intermediate workpieces from any stages. In our experiment, we choose the first step of stamping operation. That is from the sheet metal blank to the first intermediate workpieces (it is at the top-left corner in Fig. 6.8).

Since the rate of heat loss is fast in this workpiece, we can only take a total of 10 thermal infrared pictures on this intermediate workpiece with different orientations right after it is stamped. Fig. 6.9 shows six of the infrared images of the first intermediate workpiece of the cylinder.

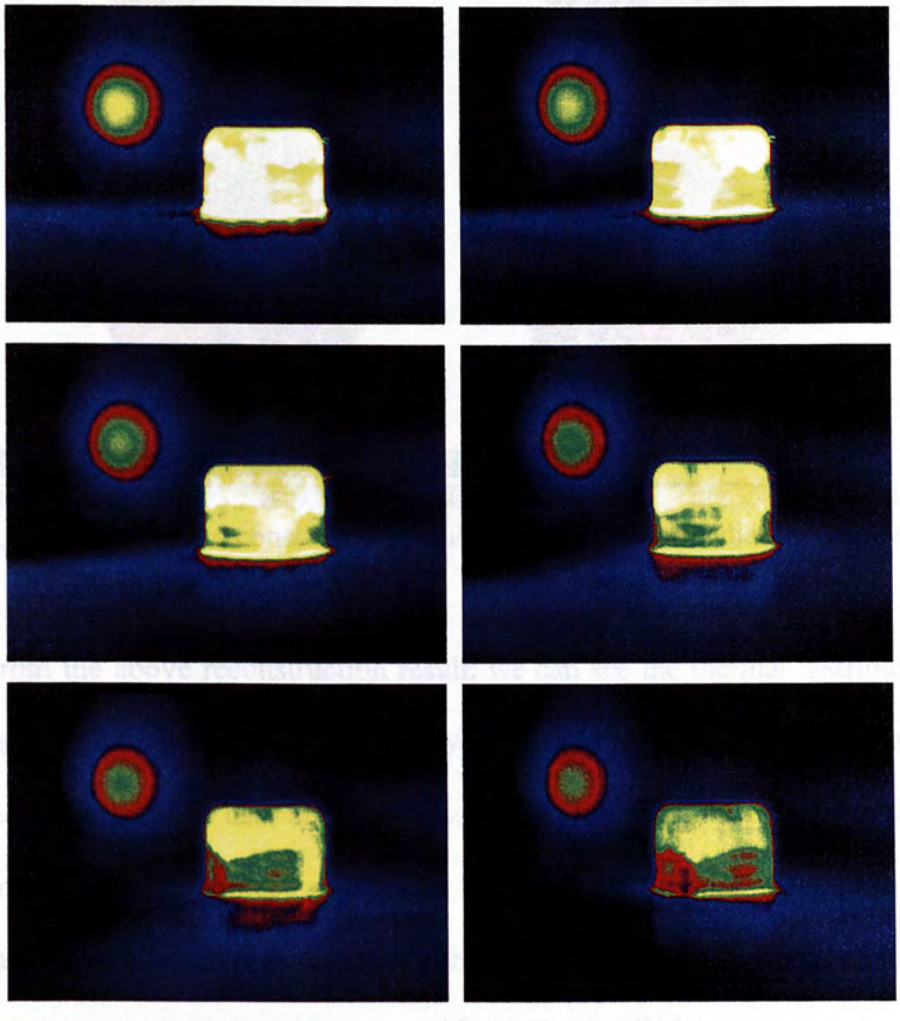

Fig.6.9 Six infrared images of the first intermediate workpiece

The reconstruction result is shown in Fig. 6.10.

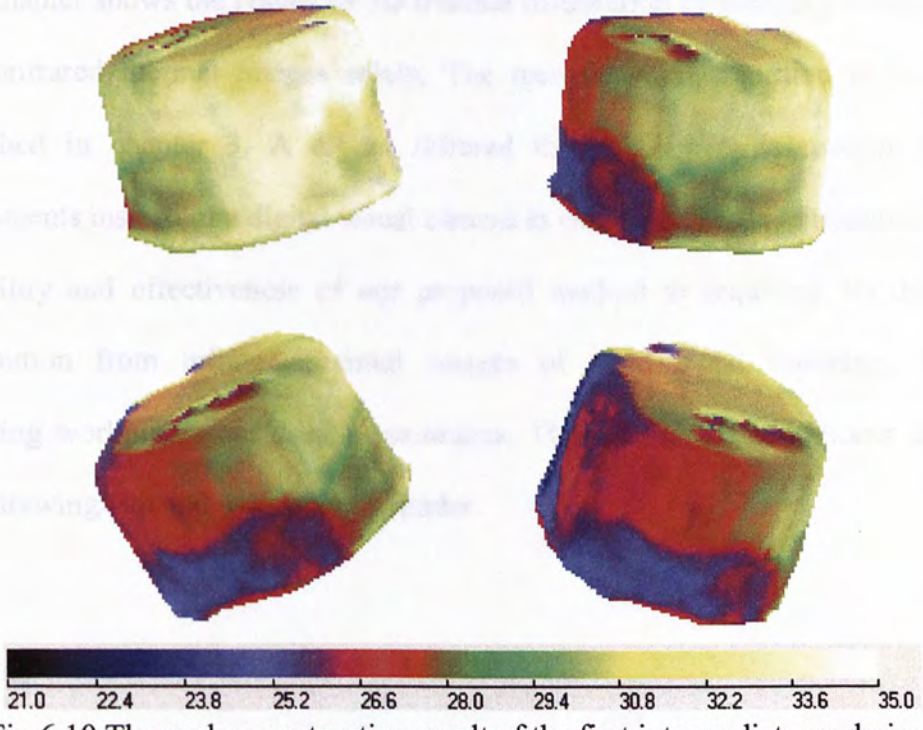

Fig.6.10 Thermal reconstruction result of the first intermediate workpiece

From the above reconstruction result, we can see the thermal distribution of the first intermediate workpiece of the cylinder right after it is stamped. Since our infrared camera has to take about 20 second for each shot, we can notice that the temperature of the wokpiece goes down from the first thermal image to the sixth thermal image. Actually, we can use either an infrared video camera or multiple infrared cameras to compensate this problem. The detailed compensation methods are discussed in chapter 8.

6.3 Summary

This chapter shows the results of 3D thermal distribution of stamping workpieces from infrared thermal images solely. The reconstruction algorithm is the one described in chapter 3. A digital infrared thermal camera is used in these experiments instead of a digital visual camera in chapter 5. The results confirm the feasibility and effectiveness of our proposed method in acquiring 3D thermal distribution from infrared thermal images of sheet metal stamping. Three stamping workpieces are used as examples. They are an air conditioner cap, a deep drawing cup and a stamping cylinder.

7. Infrared Camera on a Robotic Arm

In this chapter, the infrared camera is mounted on a robotic arm for thermal image acquisition. As we can calibrate any positions and any orientations before taking the thermal images of an object, it allows arbitrary viewpoints for thermal image acquisition rather than a pure circular sequence described in chapter 6. With arbitrary viewpoints, we can acquire more information than a circular sequence alone. The robotic arm system setup is described and a complex object (teapot) is used for illustration. Also, a comparison between the reconstruction from a circular sequence and the reconstruction from arbitrary viewpoints is shown.

With a single circular sequence of viewpoints, we can already successfully reconstruct the thermal distribution of a model. However, the main drawback of using circular motion alone is some part of the object always being invisible. Thus, the thermal information of some part of the object can not be obtained. Moreover, if some part of the object is always invisible, it does affect the shape of the reconstruction model as well. Therefore, we need arbitrary viewpoints in order to reconstruct some of the complex objects. We mount the infrared camera on a robotic arm. As we can exactly control the robotic arm to any position and orientation within the workspace, we can take thermal infrared images of objects in any arbitrary viewpoints. In this chapter, we will describe our robotic arm system setup, calibration and the reconstruction results. Finally, comparisons of

circular image sequence results and arbitrary image sequence result is given.

7.1 Robotic arm system setup

In our robotic arm system setup, we mount the thermal infrared camera on a robotic arm PERFORMER-MK3. Basically, the system setup consists of the robotic arm, the infrared camera, and a turntable. In our experiments, we place the robotic arm in two different positions and orientations. One is horizontal and the other one is inclined. Actually, we can place the camera at more positions and orientations if it is needed. Fig. 7.1 shows the robotic system setup in horizontal viewpoint to the object. Fig. 7.2 shows the robotic system setup in inclined viewpoint to the object.

Fig.7.1 The robotic system setup in horizontal viewpoint

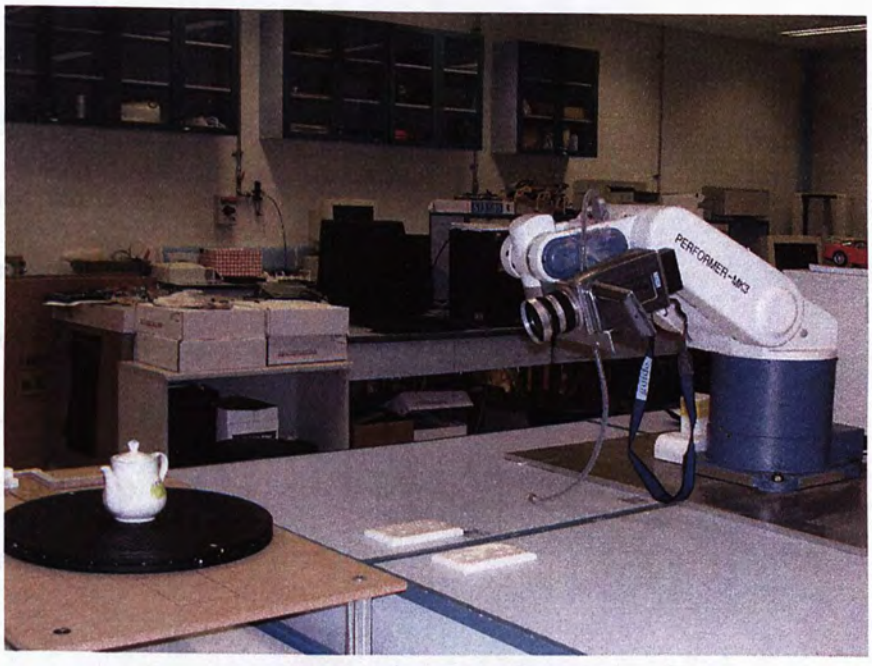

Fig.7.2 The robotic system setup in inclined viewpoint

Since the turntable can rotate 360 deg and we take 18 images for a revolution, we can now have 36 images from different viewpoints to the object. If we need more arbitrary viewpoints, we can move the robotic arm to another inclined viewpoint. As we do not want to change the intrinsic parameters (focal length) of the camera from these two different viewpoints, we maintain the distance from the object to the camera at 71 cm in these two viewpoints.

7.2 System calibration

In calibrating our robotic arm, we also use the net-and-board calibration box described in chapter 3. However, this time, we not only use the net-and-board calibration box itself, but also fill the calibration box with water. Since the plastic

cover sheet is directly attached on the surface of the box, we can further separate the rate of heat absorption between the plastic cover sheet and the net by adding water in the box. This is because water is a very high specific heat capacity substance while the net is a low specific heat capacity substance. Therefore, it provides a more reliable calibration tool as the separated rate of heat absorption can always give a good contrast between the plastic cover sheet and the net. Instead, without filling water in the box, it might give you a bad contrast of calibrating image. Fig. 7.3 shows a bad contrast of a calibrating image without filling water in the box.

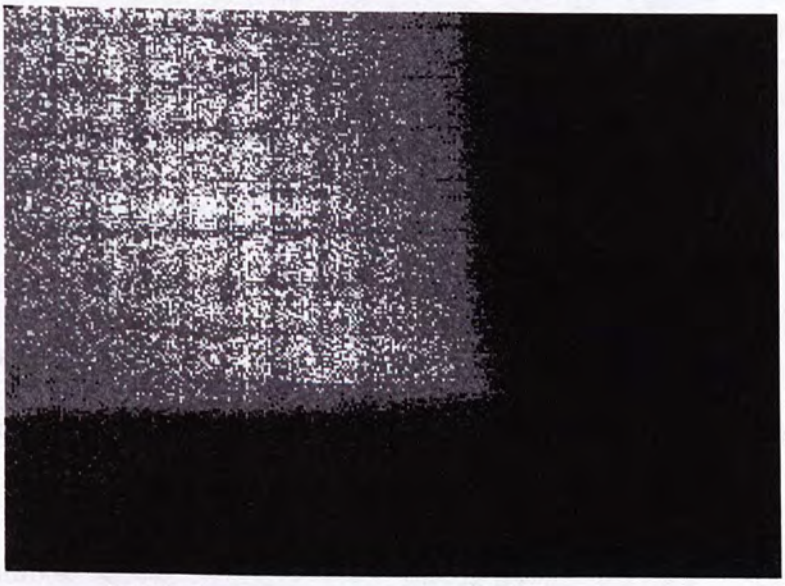

Fig.7.3 Bad contrast of a calibrating image

By filling water in the calibration box, good contrast of calibrating image can be guaranteed at any time. Fig 7.4 shows a good contrast of a calibrating image with filling water in the box.

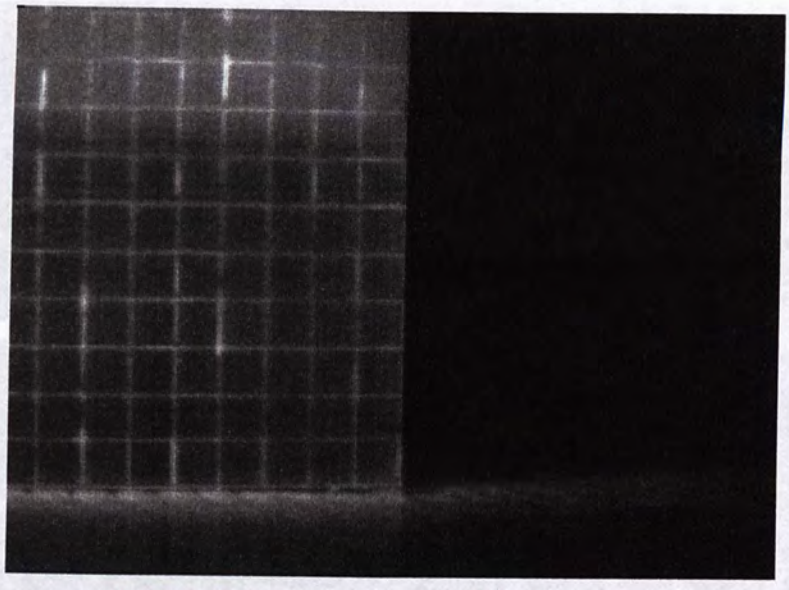

Fig.7.4 Good contrast of a calibrating image

In Fig. 7.3 and 7.4, we can clearly see the difference between a good contrast calibrating image and a bad contrast calibrating image. In a bad contrast calibrating image, it is very hard to extract the corner information and thus make the calibration difficult. Even in Fig. 7.4, we can still see the contrast of the upper two rows is not as good as the contrast of the remaining rows. This is because the water is only filled to that level. Therefore, filling water in the net-and-board calibration box can guarantee a good contrast of calibrating images.

For calibrating our robotic arm system, we use four calibrating images to calibrate the horizontal viewpoints and another four calibrating images to calibrate the inclined viewpoints. Fig. 7.5 shows the four calibrating images for the horizontal viewpoints. Fig. 7.6 shows another four calibrating images for the inclined viewpoints.

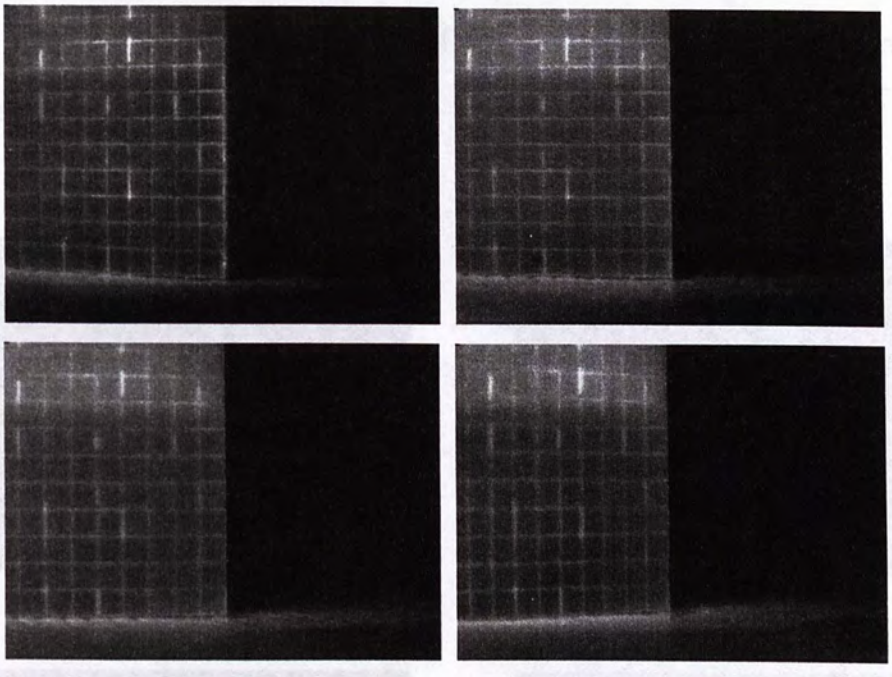

Fig.7.5 Four calibrating images for the horizontal viewpoints

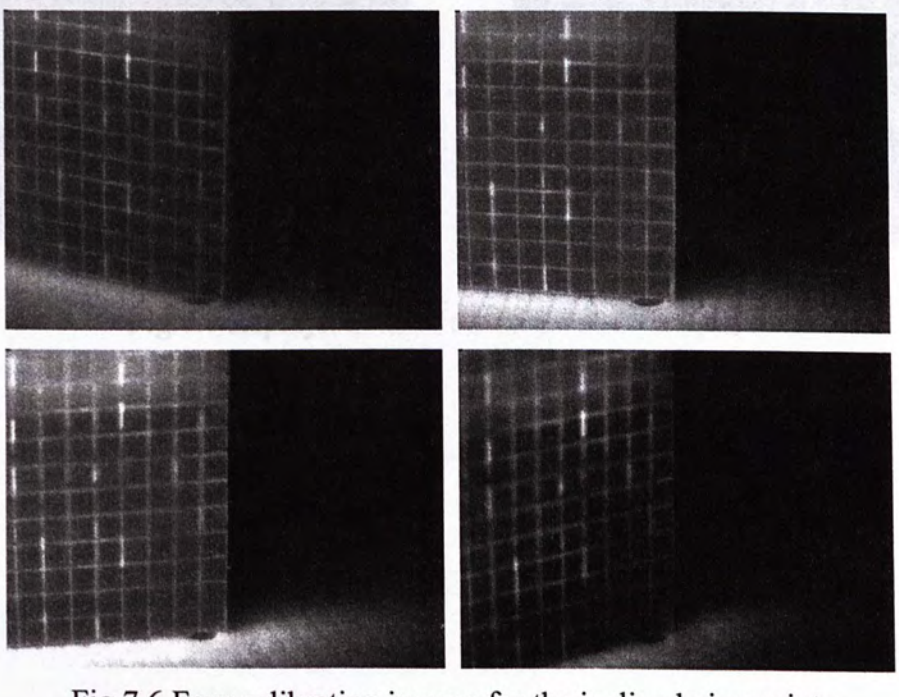

Fig.7.6 Four calibrating images for the inclined viewpoints

The reprojections of the calibrating images for the horizontal viewpoints are shown in Fig. 7.7. The reprojections of the calibrating images for the inclined viewpoints are shown in Fig. 7.8.

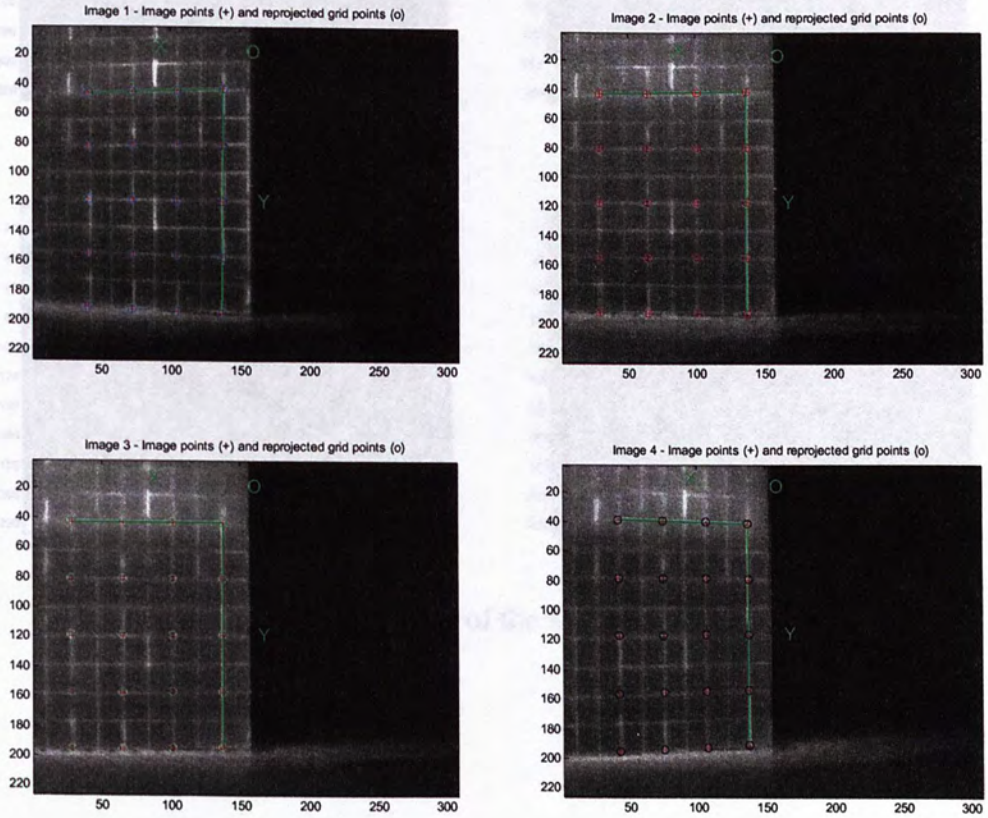

Fig.7.7 Reprojections of the horizontal viewpoints

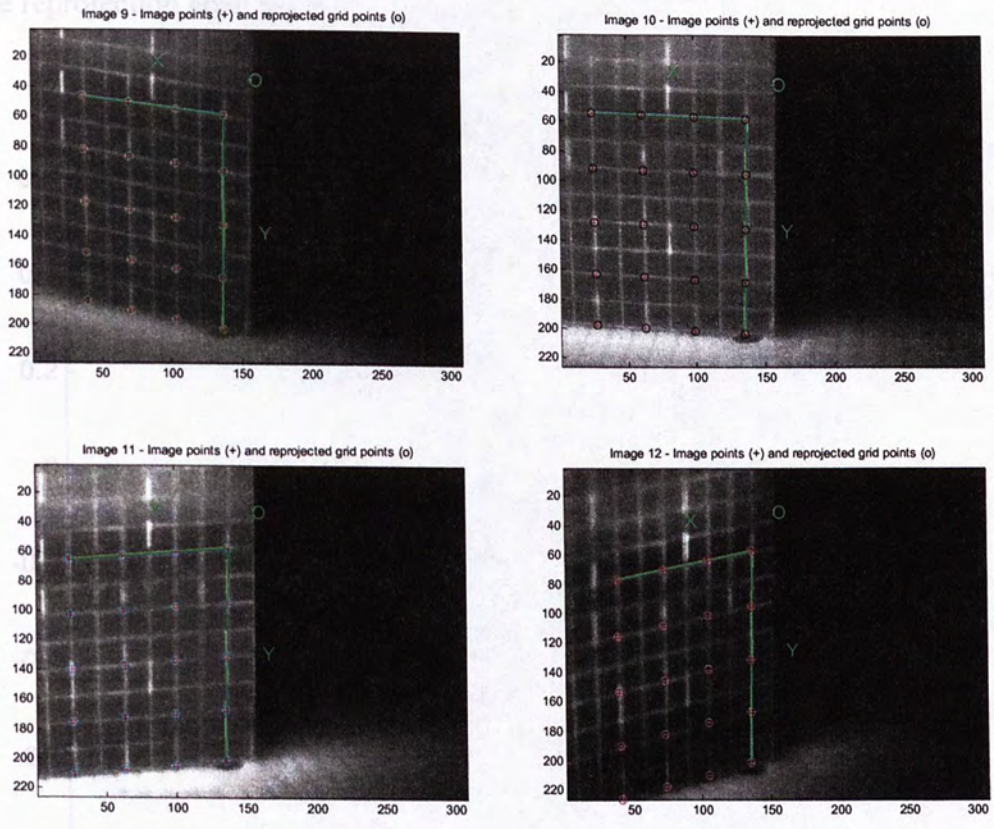

Fig.7.8 Reprojections of the inclined viewpoints

The reprojection error for these eight images is shown in Fig. 7.9.

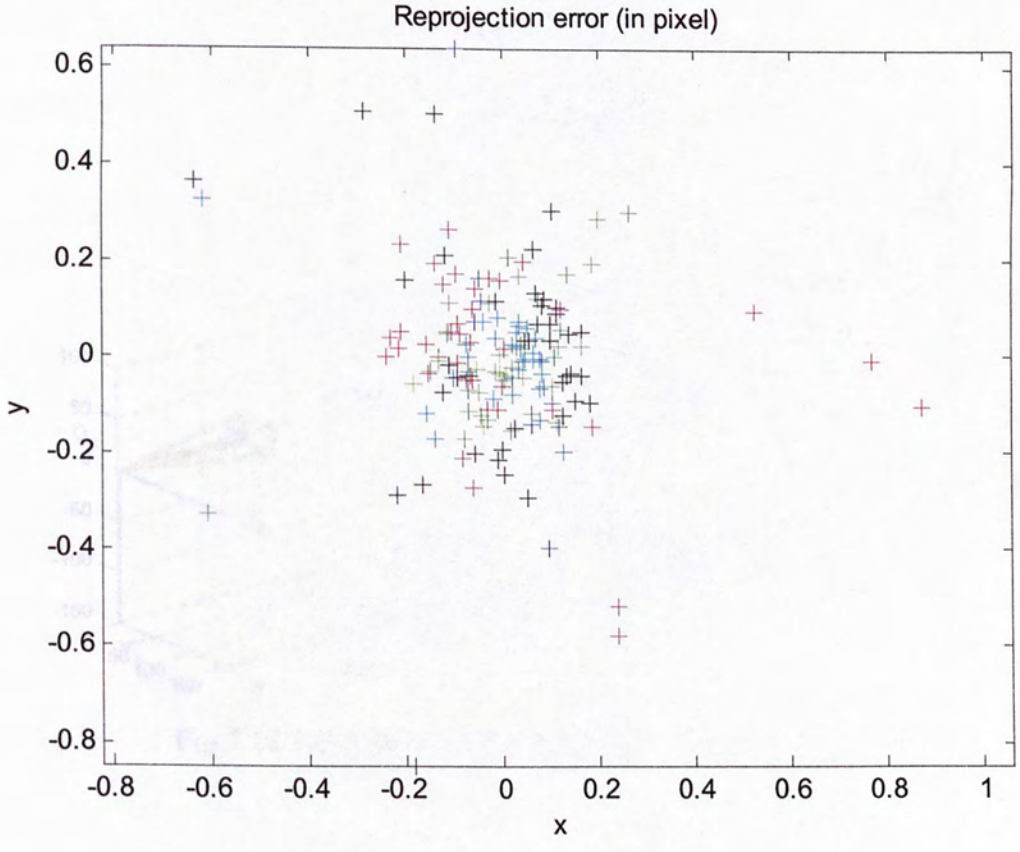

Fig.7.9 Reprojection error diagram for the images

The average reprojection error is [0.18258 0.20772] for x-direction and y-direction, respectively.

After the calibration process, the positions and orientations of the calibration box with respect to the camera is shown in Fig. 7.10.

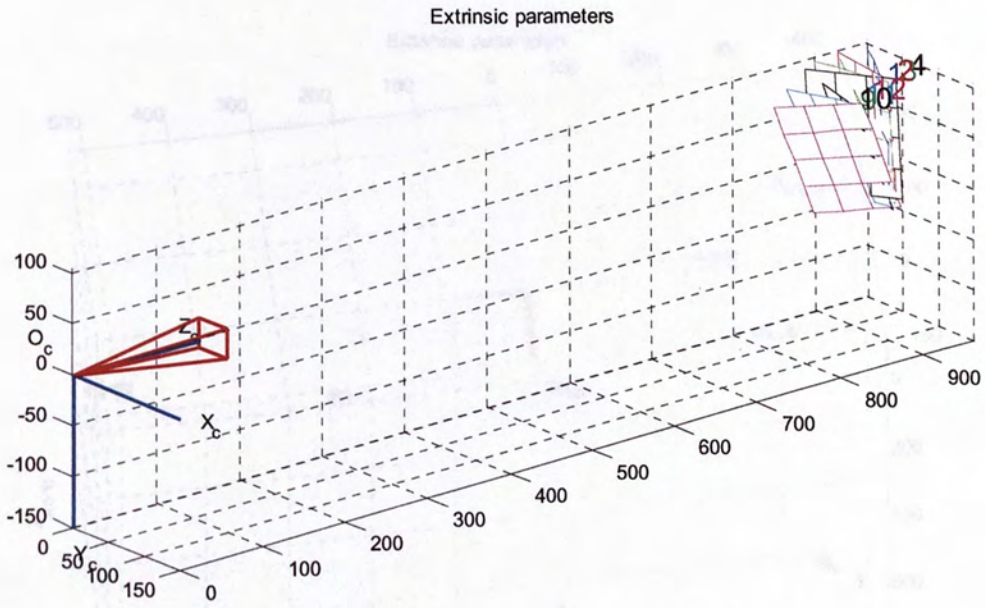

Fig.7.10 Positions and orientations of the calibration box

After the calibration process, the positions and orientations of the camera with respect to the calibration box is shown in Fig. 7.11.

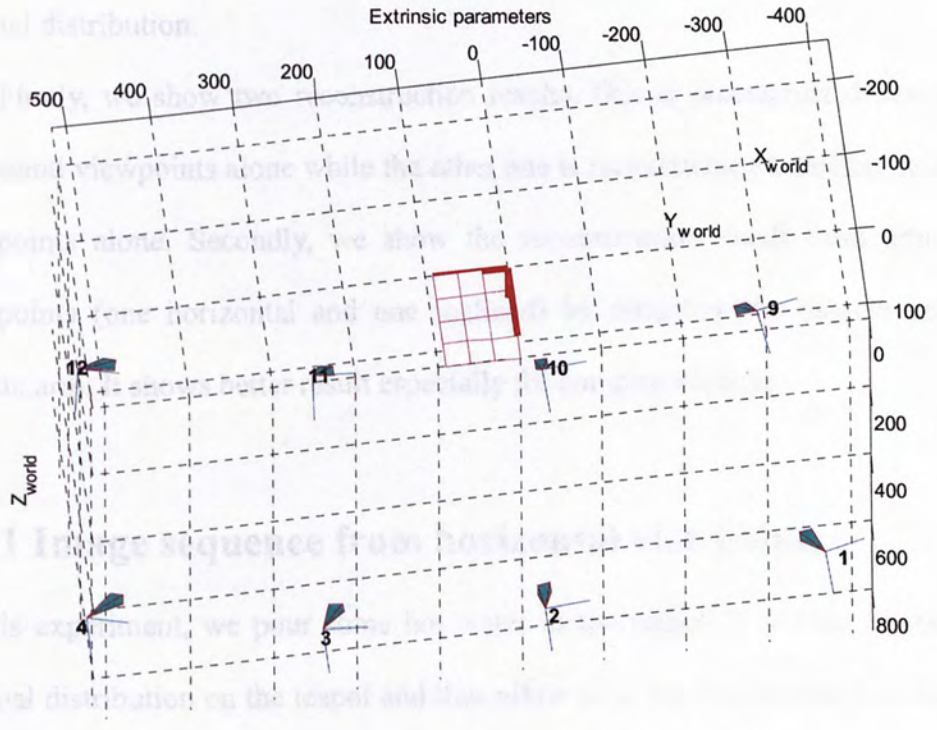

Fig.7.11 Positions and orientations of the camera

Since it is impossible to directly calibrate all the positions and orientations, the remaining positions and orientations of the infrared camera are calculated by matrix multiplication described in section 3.4.

7.3 Results

In this section, we will show several reconstruction results on a complex object (a teapot). In the experiments, we pour some hot water in the teapot for illustration of thermal distribution.

Firstly, we show two reconstruction results. One is reconstructed based on horizontal viewpoints alone while the other one is reconstructed based on inclined viewpoints alone. Secondly, we show the reconstruction result from arbitrary viewpoints (one horizontal and one inclined) by mounting the camera on the robotic arm. It shows better result especially for complex objects.

7.3.1 Image sequence from horizontal viewpoints

In this experiment, we pour some hot water in the teapot. It is used to make a thermal distribution on the teapot and thus allow us to see the thermal distribution from an infrared camera. Then we take a total of 18 thermal infrared images from horizontal viewpoints. Fig. 7.12 shows six of the infrared images from horizontal viewpoints.

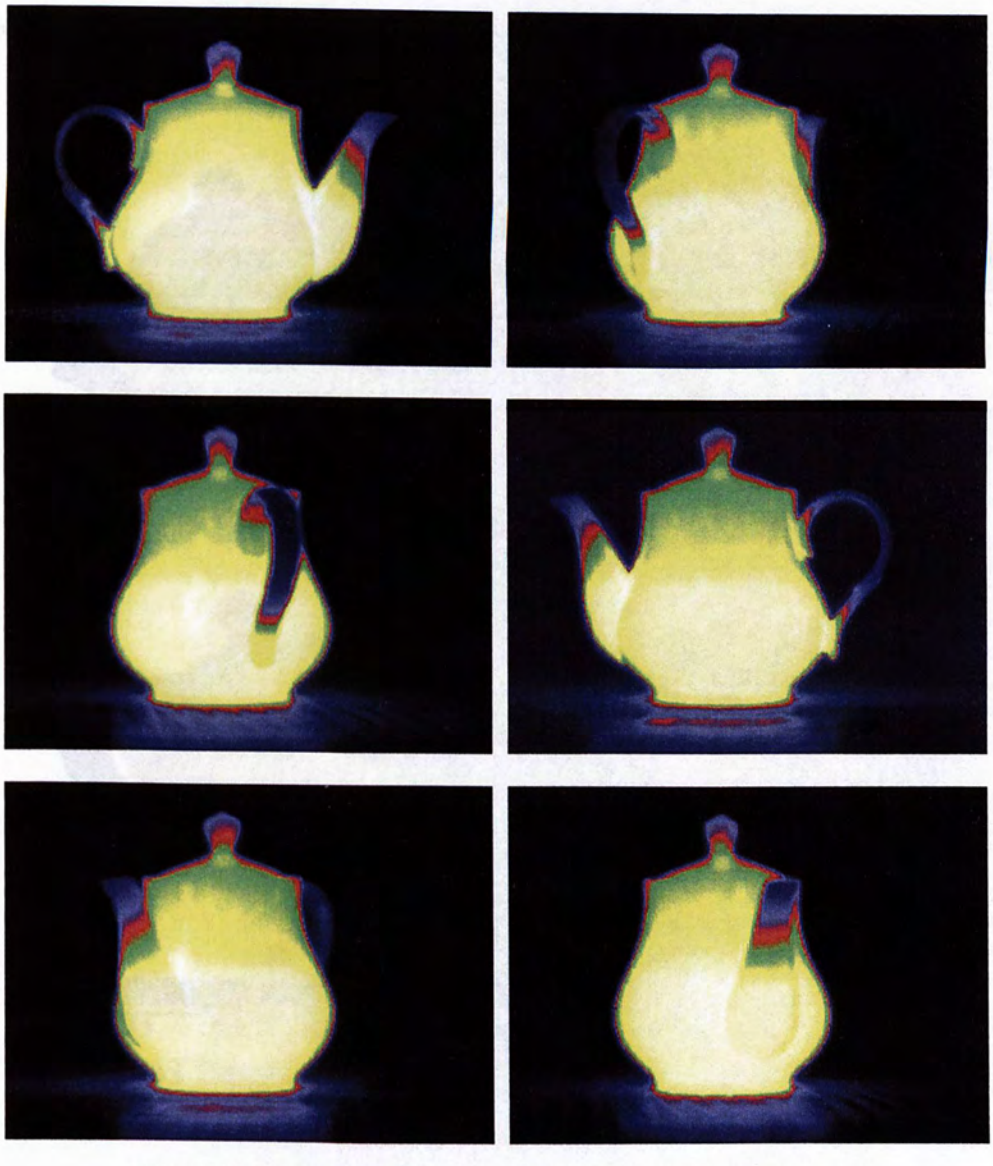

Fig.7.12 Six infrared images from horizontal viewpoints

The thermal reconstruction from horizontal viewpoints is shown in Fig. 7.13.

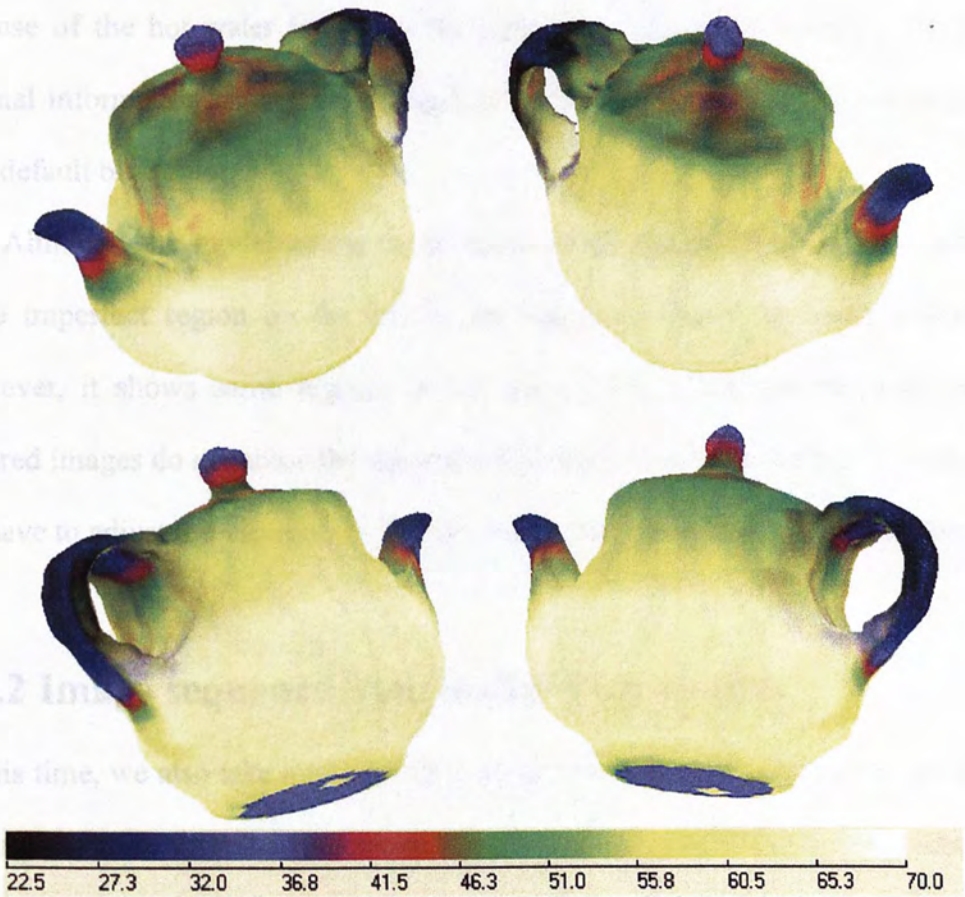

Fig.7.13 Thermal reconstruction result from horizontal viewpoints

From Fig. 7.13, we can see both the shape and the thermal distribution of the teapot. The thermal distribution of the teapot is from the lower part (hottest region because of the hot water inside) to the upper part (the coldest region). As the thermal information cannot be acquired from the infrared images, it is displayed by a default blue color.

Although the model seems to be successfully reconstructed, it still shows some imperfect region on the top of the teapot. It should be green entirely. However, it shows some regions in red color. This is because the horizontal infrared images do not show the thermal information clearly on the top. Therefore, we have to adjust the viewpoints. We can incline the viewpoints by some angles.

7.3.2 Image sequence from inclined viewpoints

In this time, we also take a total of 18 thermal infrared images. However, we take the images from inclined viewpoints. Fig. 7.14 shows six of the infrared images frominclined viewpoints.

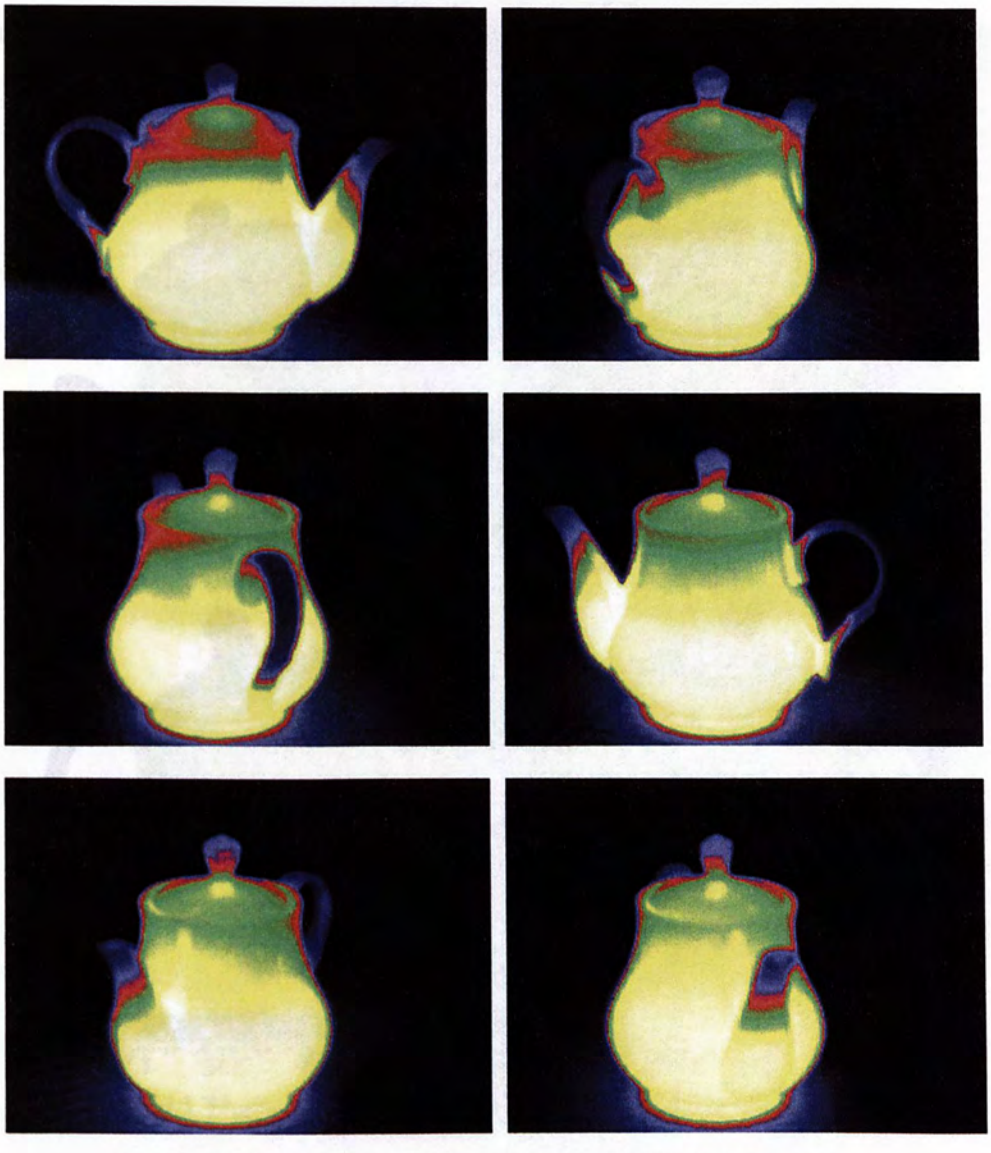

Fig.7.14 Six infrared images from inclined viewpoints

The thermal reconstruction result from inclined viewpoints is shown in Fig. 7.15.

Fig.7.15 Thermal reconstruction result from inclined viewpoints

From Fig. 7.15, we can also see both the shape and the thermal distribution of the teapot. The thermal distribution of the teapot is from the lower part (hottest region because of the hot water inside) to the upper part (the coldest region). In this reconstruction result, we can see a evenly distributed green color on the top and thus solve the problem encountered in horizontal viewpoints.

Although the model seems to be successfully reconstructed, it still shows

some imperfect region on the bottom of the teapot this time. It should be flat However, it shows a cone-shaped structure. This is because of the perspective projection of the camera and the reconstruction method. Therefore, we have to adjust the viewpoints to horizontal in order to carve out the unwanted cone-shaped structure. However, as mentioned previously, the result from horizontal viewpoints shows imperfect region on the top of the teapot. Obviously, there is a compromise between the imperfect region on the top of the teapot from horizontal viewpoints alone and the imperfect structure on the bottom of the teapot from inclined viewpoints alone. As a consequence, we mount the camera on the robotic arm so that we can take images at any calibrated arbitrary viewpoints as we can control the robotic arm to the calibrated positions and orientations. By mounting the camera on a robotic arm, we can incorporate both the horizontal viewpoints and the inclined viewpoints for reconstruction. We can even incorporate more inclined viewpoints for reconstruction in order to have a better reconstruction result.

7.3.3 Image sequence from arbitrary viewpoints

To achieve arbitrary viewpoints image capture, we can mount the camera on a robotic arm. Thus, we can incorporate both the 18 horizontal viewpoints and the 18 inclined viewpoints together for better reconstruction. Fig. 7.16 shows the thermal reconstruction result from arbitrary viewpoints.

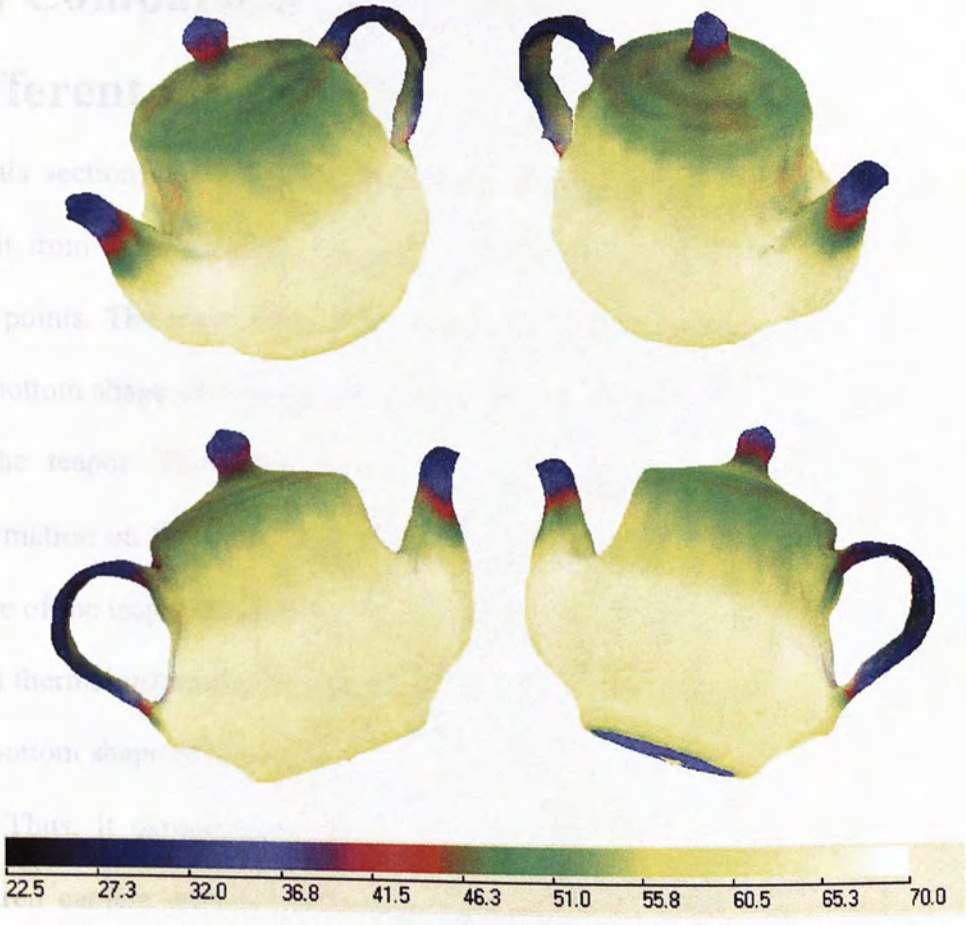

Fig.7.16 Thermal reconstruction result from arbitrary viewpoints

From Fig 7.16, we can see that the result has neither the imperfect region on the top of the teapot nor the imperfect structure on the bottom of the teapot. Therefore, it demonstrates the success of our approach on mounting the camera on a robotic arm.

7.4 Comparison of the three different viewpoints

In this section, we will compare the three reconstruction results. They are the result from the horizontal viewpoints, the inclined viewpoints and the arbitrary viewpoints. The result from the horizontal viewpoints gives a good structure on the bottom shape of the teapot but gives imperfect thermal information on the top of the teapot. The result from the inclined viewpoints gives good thermal information on the top of the teapot but gives imperfect structure on the bottom shape of the teapot. In contrast, the result from arbitrary viewpoints not only gives good thermal information on the top of the teapot but also gives good structure on the bottom shape of the teapot.

Thus, it demonstrates the success and the effectiveness of mounting the infrared camera on the robotic arm for thermal distribution reconstruction. Fig 7.17 shows the reconstruction results from the horizontal viewpoints, inclined viewpoints and arbitrary viewpoints at the same time.

Fig.7.17 Comparison of three different viewpoints
(top: horizontal ; middle: inclined ; bottom: arbitrary)

7.5 Summary

In this chapter, the infrared camera is mounted on a robotic arm for thermal image acquisition. As we can calibrate any positions and any orientations before taking thermal images of an object, it allows arbitrary viewpoints for thermal image acquisition rather than a pure circular sequence described in chapter 6. The system is described and a teapot is used for illustration. Also, a comparison between the reconstruction from a circular sequence and the reconstruction from arbitrary viewpoints is shown.

8. Compensation of Temperature Fade-out Problem

8.1 Causes of temperature fade-out

From the thermal infrared images of the stamping workpieces right after stamping, we can see that the temperature is cooling down from image to image or say from time to time. This is because the heat is lost to the surroundings. After the stamping operation, the heat is generated by the plastic deformation of the sheet metal. After the stamping operation, however, there is no continuous heat source to maintain the heat transfer equilibrium. Therefore, the heat is gradually lost to the environment. This is the temperature fade-out problem. A time sequence of the thermal infrared images of the sheet metal workpieces (stamping cylinder from KS factory) right after stamping is shown in Fig. 8.1

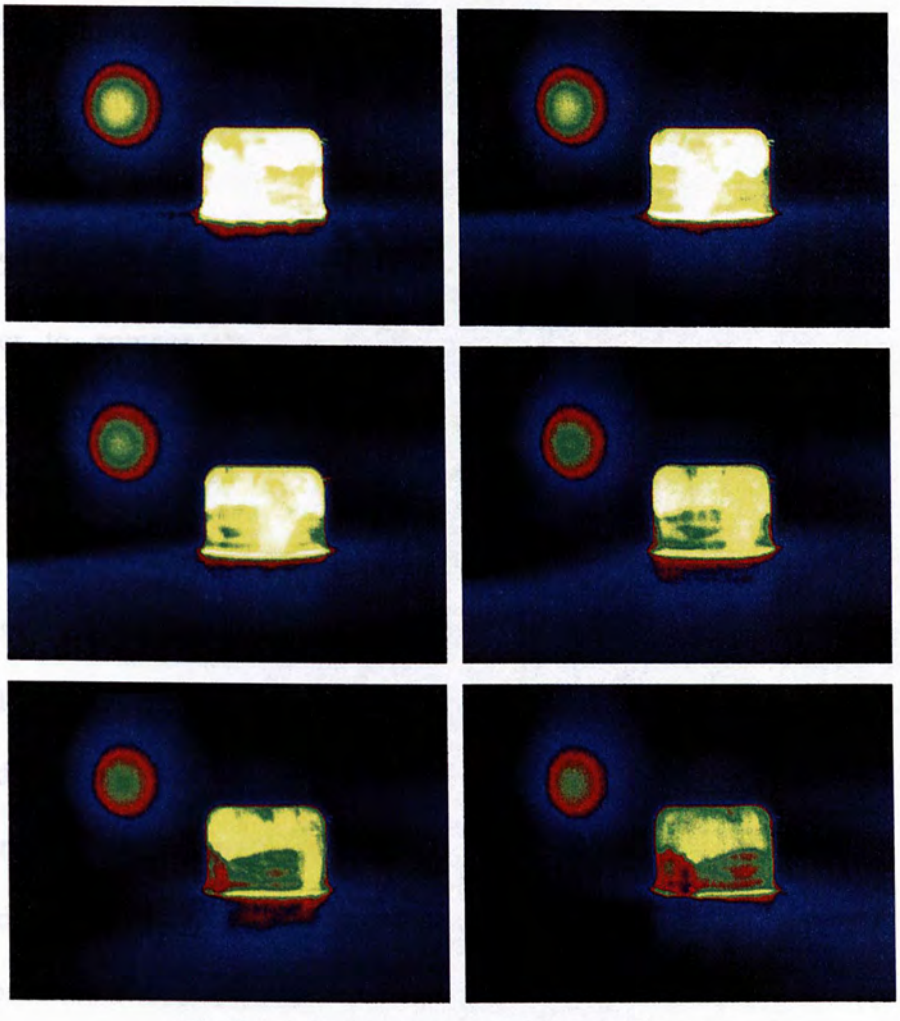

Fig.8.1 A time sequence of thermal images
showing temperature fade-out

However, this problem only exists in the stamping workpieces shown in section 6.2.3, but not in the Ferrari car model described in chapter 9. It will be described in details in chapter 9. In the Ferrari car model, there is a continuous heat source in the engine cavity in order to simulate the thermal distribution of a car after the engine is turned on. Because of the heat source inside, the equilibrium

can be established between the heat generated by the heat source and the heat loss to the surroundings. Therefore, we do not seek this problem in this application and it can be perfectly used in the automobile industries.

8.2 Solutions

In order to compensate this temperature fade-out problem, there are two approaches. We can either use one of them. They are hardware approach and computational approach.

In the hardware approach, as the temperature fade-out problem is due to the heat loss over time, we can reduce the image capturing time by using multiple thermal infrared cameras or a video infrared camera. By using multiple thermal infrared cameras, we can take several images at a time. Thus, it reduces the capturing time according to the number of infrared cameras. By using a video infrared camera, it can capture 20-30 frames per second. Therefore, we can rotate the model on a turntable for less than a second in order to get a sequence of images from all views. In this short period of time, the temperature fade-out problem can be greatly reduced.

In the computational approach, we can use FEA to simulate the 3D thermal distribution of a workpiece over time after stamping operation by considering heat transfer (conduction within the workpiece, convection and radiation). Originally, we intended to reduce the temperature fade-out problem from the captured thermal infrared images. However, as the thermal image is a 2D picture and it

does not indicate anything about the environment (ambient temperature, air flow and etc), geometry of the workpiece, and material properties. As this information is very important to the heat transfer (by conduction, convection and radiation), it is very difficult or even impossible to compensate the temperature fade-out problem from the captured infrared images alone. Alternatively, we suggest using FEA to simulate the thermal distribution over time. As we can define the initial conditions, such as ambient temperature, air flow, geometry of the workpiece, material properties and etc, we can compute the thermal distribution straightforwardly from FEA rather than inversely from captured thermal infrared images.

8.3 Summary

This chapter explains the problem of temperature fade-out and how the problem affects the 3D thermal reconstruction result. Temperature fade-out means the gradual decrease of the temperature on an object due to heat loss to the surroundings and heat conduction within an object. In this chapter, it also describes how we can solve the problem.

9. Other Applications

In this chapter, other possible applications in industries are discussed. It is especially beneficial to automotive industry and general heat transfer analysis. Experimental verification with heat transfer Finite Element Modeling (FEM) results could be carried out in industries. The 3D thermal reconstruction result of a car body is shown.

9.1 Automotive industry

Thermal analysis using Finite Element Modeling (FEM) is widely used in automotive industry nowadays. FEM can give simulation results at design stage. However, as FEM is a kind of simulations, it normally suffers from deviations with experimental results. Therefore, experimental measurement is necessary. To measure the 3D temperature distribution on a car body, we normally use a number of temperature sensors and then record the temperature values according to the positions of the sensors. It can provide the temperature values at different positions. Using this information, we can obtain the 3D temperature distribution on a car body. However, this method is time consuming and inconvenient, as we have to place a number of sensors on a car body, measure its corresponding positions as well as process the measured temperature values.

In contrast, we firstly take a sequence of 2D thermal infrared images of the car body to have 2D temperature distribution and then reconstruct the 3D

temperature distribution from the 2D images using computer vision method. It provides a more convenient method to acquire 3D temperature distribution compared to using a number of temperature sensors. The experimental results show the feasibility of our method.

9.1.1 Background

Nowadays, Finite Element Modeling (FEM) is widely used to compute 3D thermal distribution for heat transfer analysis in various kinds of industrial applications, especially in automotive industry. It involves analysis of 3D thermal distribution of electrical machine [38, 39], turbogenerator [40, 41], motor [42], vehicle cabin [43], vehicle body [44, 45, and 46] and etc. It actually plays an important role in predicting the improper design during the initial stage. However, as FEM is a kind of simulations, it does not give any cues on improper making and improper operation on final outcomes in reality at the testing and verification stage. As a consequence, it leads to a large research topic on measurement and information acquisition.

To acquire 3D thermal distribution of a vehicle body, the best way is placing a number of temperature sensors on the vehicle body with known position of each sensor [10]. Then we can record the temperature values of each sensor and process the values with the positions of each sensor to obtain the 3D temperature distribution. However, it is extremely time consuming and inconvenient. In contrast, we use an infrared camera to acquire a sequence of 2D thermographic

images and then reconstruct the 3D temperature distribution from the captured 2D thermal images by computer vision method. By using our approach, it can not only avoid using large number of sensors but also avoid measuring all the sensors positions. In this section, we put a heat source in the engine cavity of a Ferrari car model to imitate the temperature distribution of the car body after the engine is turned on in reality. Then we acquire the 3D temperature distribution of the vehicle body using our proposed method.

9.1.2 Experiment and result

In our experiment, we put a heat source (chemical warmer) in the engine cavity of a Ferrari car model to imitate the temperature distribution of a vehicle body after the engine is turned on in reality. The thermal infrared images are taken after 15 min for ensuring that the heat transfer is in steady state. We totally take 18 thermal infrared images of the Ferrari car model with 20 deg interval between each image. Fig. 9.1 shows the Ferrari car model in our experiment.

Fig.9.1 The Ferrari car model

Fig. 9.2 shows nine out of 18 thermal infrared images of the car model with 40 deg interval between each image. Fig. 9.3 shows the reconstruction of 3D temperature distribution of the car body.

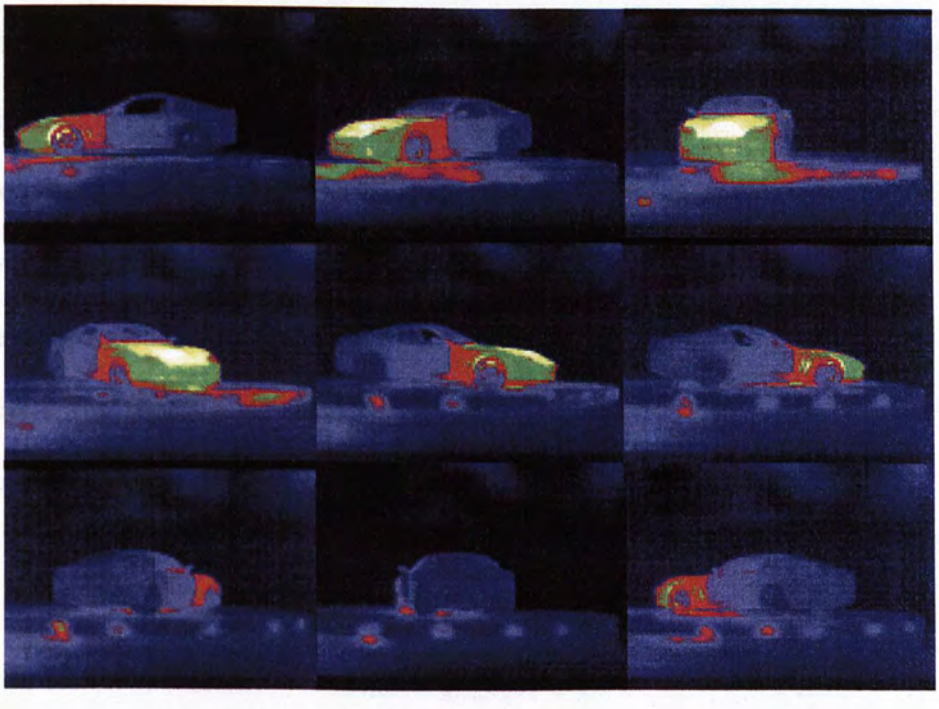

Fig.9.2 The nine out of 18 infrared images of the car model

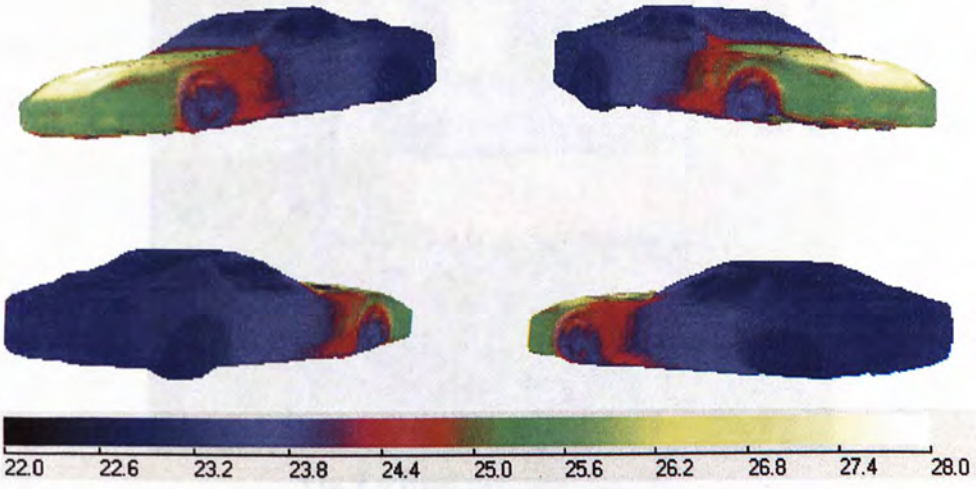

Fig.9.3 The 3D thermal distribution of the car body

The color differences imply the differences on the surface temperature of the Ferrari car body. The temperature reading is in degree Celsius. It clearly shows both of the 3D perception and the temperature distribution of the car body. We can see the heat transfer from the engine to the whole car body. It demonstrates the quality of the result and confirms the effectiveness and practicality of our method in acquiring 3D temperature distribution without using a large number of temperature sensors. To acquire 3D temperature distribution of a real car, we can use a larger net-and-board calibration box for system calibration and a real car turntable for rotation or multiple infrared cameras. Fig. 9.4 shows a real car turntable.

Fig.9.4 Real car turntable [47]

This section presents a complete and practical system for 3D temperature distribution acquisition without using a large number of temperature sensors. It is especially beneficial to thermal analysis in automotive industry. The experimental result demonstrates the effectiveness and practicality of our method.

9.2 General heat transfer analysis

Since we have shown different kinds of thermal distribution reconstruction results, such as stamping workpieces, teapot and car body, this technology can be applied to any objects. Therefore, it can be used for general heat transfer analysis. Normally, we can use the technology to acquire the experimental thermal distribution and then compare it with the FEA result for system verification.

9.3 Summary

In this chapter, other possible applications in industries are discussed. It is especially beneficial to automotive industry and general heat transfer analysis. Experimental verification with heat transfer Finite Element Analysis (FEA) results could be carried out in industries. The 3D thermal reconstruction result of a car body is shown.

10. Conclusions

This chapter presents a summary on this thesis. It describes the main ideas from the need and the motivation of this project to the approach of the problem, from the implementation of the system to the experimental results, and from the compensation of temperature fade-out problem to the other application areas.

Then the main contributions of the thesis are listed. It consists of the implementation of the diagnosis system for sheet metal stamping, the proposal of net-and-board calibration box for infrared thermal cameras, the breakthrough of 3D thermal distribution acquisition from thermal images alone, the suggestions on the compensation of temperature fade-out problem, and the study of application in automotive industry. Finally, it concludes with possible areas for future research.

10.1 Summary

In this thesis, we have presented a complete and practical system for the acquisition of 3D thermal distribution in sheet metal forming using infrared thermography and computer vision techniques. Since it is impossible to place numerous temperature sensors on the sheet metal blank before it is stamped, we take a infrared thermography and computer vision approach to the problem. It can be seen as an experimental thermal measurement system to optimize sheet metal forming processes and to make a process more close to limitations of the material properties. It can reconstruct both the geometric information and the thermal

distribution information from infrared images alone. Moreover, it is especially beneficial to the areas of surface thermal analysis of automotive and manufacturing applications.

In the past, to diagnose stamping operation, we normally compare the experimental strain distribution of the workpiece acquired from the deformation of the grid pattern with the simulation result from finite element modeling. However, this is extremely time consuming as we have to etch the sheet metal blank before the stamping operation. Therefore, we propose to diagnose the stamping operation based on thermal energy distribution since the similarity between the strain distribution and the thermal distribution. This is because most of the plastic deformation energy converts to the heat energy. By analyzing the thermal energy, we are able to pin point where the problem is in stamping operation. As this method is designed to pin-point where the problem is, but not for online applications like monitoring, time (fast enough to keep up with production) is not a concern. Indeed, it allows a new tool (i.e. thermal distribution) for trained engineers to diagnose sheet metal stamping problems that cannot be seen before. It should also be pointed out that the transfer of the workpiece before thermal analysis could affect the diagnosis. However, it is not difficult to place our system next to the stamping machine to eliminate the problem. Also, we can simulate a time-variant heat FEA result to compensate this factor.

To acquire 3D thermal distribution, we can place a number of temperature sensors on the object. However, it is impossible to place the sensors on a sheet metal blank as it is going to be fed in a stamping machine. Thus, we take

thermography approach to this problem. Basically, we can use a combination of laser scanner and an infrared camera to tackle this problem. However, laser scanners are extremely expensive, and it costs around US$50,000 a piece. We can also use a stereo pair of visual cameras and an infrared camera to tackle this problem. However, it is only applicable to corner-typed objects or textured objects and most of stamping workpieces are smooth and textureless. Therefore, it fails to work in stamping applications. In this thesis, we combine octree carving technique from Szeliski and thermography technology to reconstruct the geometric shape of stamping workpieces. By using this method, we can use infrared camera alone to acquire 3D thermal distribution of a smooth and textureless stamping workpiece.

To implement the diagnosis system, infrared camera calibration is a big issue. Since conventional checkerboard cannot be seen by an infrared camera, it is impossible to calibrate an infrared camera. Therefore, we propose different calibration method for infrared cameras. They are LEDs calibration board and net-and-board calibration box. We found that the net-and-board calibration box perform extremely well in calibrating infrared cameras. After calibrating the infrared cameras, we can use octree carving technique to reconstruct the thermal distribution model.

Since no one use infrared camera to reconstruct an entire thermal distribution of an object, we have to make sure that the experiment would not be affected by the environment. We propose the validation resistor box to ensure that the experiment is in an omni-directional infrared environment and suitable for data acquisition.

After processing the data, the thermal reconstruction results are shown. It involves several stamping workpieces. In addition, mounting the infrared camera on a robotic arm is proposed. It shows better result than using a tripod alone. This is because some part of the object is always invisible during a single circular sequence. Therefore, mounting the infrared camera on a robotic arm gives arbitrary viewpoints and thus solves the problem.

As the temperature is continuously losing to the surroundings and causes the temperature fade-out problem, we suggest several methods to reduce this unwanted effect. We can either use multi infrared cameras or an infrared video camera to reduce this effect. Alternatively, we can also model the FEA result from time to time. This is called time-variant thermal FEA result.

Besides the stamping application, we also investigate other possible applications. We use this technology to reconstruct a car body. It shows a promising result, and we believe that it can be applied to automotive industry for heat transfer analysis.

In summary, we did demonstrate the effectiveness and practicality of our proposed method on the acquisition of 3D thermal distribution and it shows promising results. The main contributions of this thesis are listed below.

Contributions:

1. A diagnosis system for stamping operations based on thermal energy distribution. This method can avoid the time consuming grid pattern preparation in the traditional sheet metal stamping diagnosing method.
2. A net-and-board calibration box for infrared cameras. Since a conventional

checkerboard cannot be seen by infrared cameras, it fails to calibrate infrared cameras. With our proposed net-and-board calibration box, it allows the calibration of infrared cameras.

3. Reconstruction of 3D thermal distribution from infrared images alone. We neither have to use any laser scanner nor a stereo pair of visual cameras to reconstruct the 3D thermal distribution. Also, it can apply to smooth and textureless stamping workpieces while stereo method does not.
4. Suggestions on the compensation of temperature fade-out problem. We suggest using multi infrared cameras or an infrared video camera to reduce the image capturing time. Thus, the temperature fade-out problem can be reduced. Also, it is possible to simulate a time-variant heat FEA result to compensate the temperature fade-out problem.
5. A study of possible application in automotive industry. We use our acquisition system to successfully reconstruct a 3D thermal distribution of a car body. It can be used for heat transfer analysis of vehicles in automotive manufacturing.

After summarizing what we have contributed, we would like to discuss some of the limitations of the reconstruction method. By using octree carving reconstruction, i.e. silhouette-based 3D reconstruction, it is impossible to reconstruct concavities of objects. Also, for non-curved objects with real edges concavities, the reconstruction result greatly depends on the placement of cameras if only several images are taken. For example, a square object becomes an octagon if only four images are taken from the extension of the four corners of the square

object [48]. For self-occlusion problem, since this is not a stereo matching method, feature existing in an image but not another does not matter in octree carving method. This is because we do not need to find out the correspondences between images. However, if there is an area that is always occluded in the image sequence, we can do nothing on it so as all other reconstruction methods. Therefore, camera placement plays an important role in silhouettes-based 3D reconstruction and it does affect the reconstruction result. In the camera placement, we have to find out an image sequence that makes the least occurrence of concavities viewpoints and self-occlusions.

10.2 Future work

In future, we can work on several directions in the diagnosis of sheet metal stamping based on thermal energy distribution. Firstly, we can work on the relationship between the process variables and the thermal distribution using Monte Carlo simulation. This can allow the experienced engineers to identify the problems more accurately since engineers can directly refer to the potentially-problematic process variables. Secondly, we can work on the optimization of stamping processes and die design based on the diagnosis. Although we can diagnose where and how the problems are, we still have to find out the possible ways to solve the problems. Now, our team is focusing on the optimization of the die and the process after knowing the problems from the diagnosis system. In other words, it is the ways to modify the die and the process

parameters. Finally, modeling of time-variant thermal FEA in stamping processes could be carried out.

For the 3D thermal distribution acquisition, however, it has a same limitation as all silhouette-based volumetric reconstruction algorithms, such as the inability to reconstruct concavities of an object. As thermal infrared images contain little textured information, combination of silhouette-based reconstruction, feature-based reconstruction and space carving reconstruction [48] in thermal infrared images could be a future research direction.

A. Transformation Matrices of the System

In the transformation matrices of the system, the projection matrix $\mathbf{P}_1$ is for the first camera. It can be decomposed into the camera calibration matrix $\mathbf{K}$, the rotation matrix $\mathbf{R}$ and the translation vector $\mathbf{t}$ as follows

$$\mathbf{P}_1 = \mathbf{K}[\mathbf{R} \quad \mathbf{t}] \tag{A.1}$$

The rotation matrix $\mathbf{R}$ and the translation vector $\mathbf{t}$ are describing the transformation between the camera and the calibration box. For the rotation matrix $\mathbf{R}$, we can further decompose it as follow

$$\mathbf{R} = \begin{bmatrix} \mathbf{X}\cdot\mathbf{X}_c & \mathbf{Y}\cdot\mathbf{X}_c & \mathbf{Z}\cdot\mathbf{X}_c \\ \mathbf{X}\cdot\mathbf{Y}_c & \mathbf{Y}\cdot\mathbf{Y}_c & \mathbf{Z}\cdot\mathbf{Y}_c \\ \mathbf{X}\cdot\mathbf{Z}_c & \mathbf{Y}\cdot\mathbf{Z}_c & \mathbf{Z}\cdot\mathbf{Z}_c \end{bmatrix} \tag{A.2}$$

where $\mathbf{X},\mathbf{Y},\mathbf{Z}$ are the principal vectors of the calibration box orientation and $\mathbf{X}_c,\mathbf{Y}_c,\mathbf{Z}_c$ are the principal vectors of the camera orientation. For the translation vector $\mathbf{t}$, we can further decompose it as follow

$$\mathbf{t} = \begin{bmatrix} t_x \\ t_y \\ t_z \end{bmatrix} \tag{A.3}$$

where t_x, t_y, t_z are the coordinate values of the origin of the calibration box

with respect to the camera coordinate frame. Fig.A.1 shows the orientation and position of the calibration box at a certain viewpoint. Fig A.2 shows the image of the calibration box from the camera.

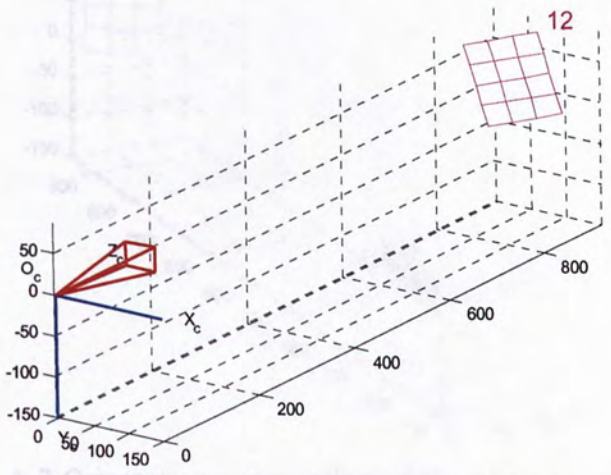

Fig.A.1 Orientation and position of the calibration box

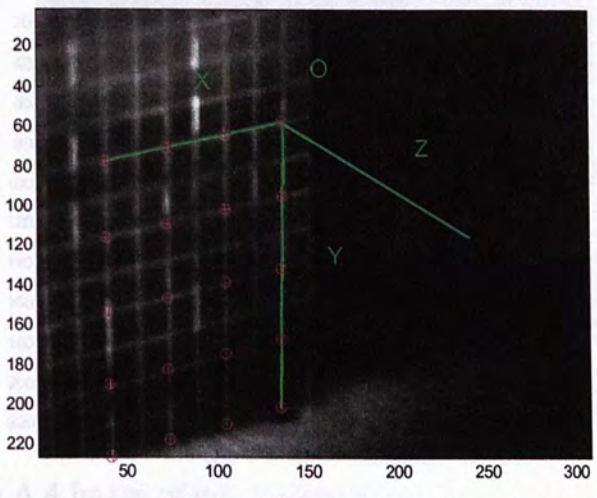

Fig.A.2 Image of the calibration box from the camera

From this example, $\mathbf{R} = \begin{bmatrix} -0.8738 & 0.0270 & 0.4855 \\ 0.2001 & 0.9299 & 0.3085 \\ -0.4432 & 0.3667 & -0.8180 \end{bmatrix}$ and $\mathbf{t} = \begin{bmatrix} 91.9337 \\ -86.8201 \\ 878.3968 \end{bmatrix}$

Fig.A.3 shows the orientation and position of the calibration box at another viewpoint. Fig A.4 shows the image of the calibration box from the camera.

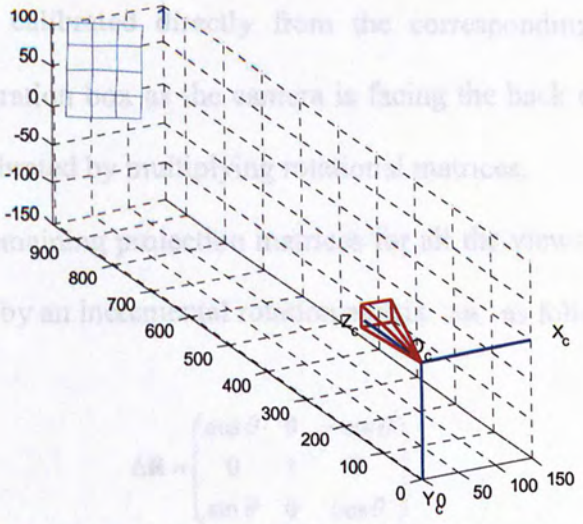

Fig.A.3 Orientation and position of the calibration box

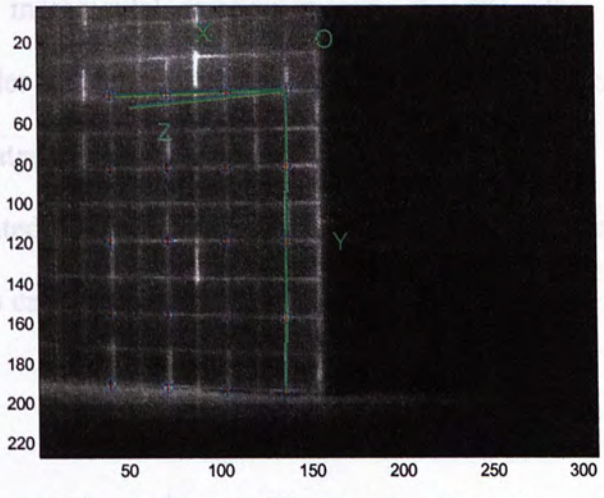

Fig.A.4 Image of the calibration box from the camera

From this example, $\mathbf{R} = \begin{bmatrix} -0.8628 & -0.0028 & -0.5056 \\ -0.0298 & 0.9985 & 0.0453 \\ 0.5047 & 0.0541 & -0.8616 \end{bmatrix}$ and $\mathbf{t} = \begin{bmatrix} 94.6994 \\ -100.7777 \\ 903.3302 \end{bmatrix}$

Since it is not always possible to see the front face of the net-and-board calibration box when performing a complete rotation on a turntable, some of the views can not be calibrated directly from the corresponding images of the net-and-board calibration box as the camera is facing the back of the box. Thus, these views are calibrated by multiplying rotational matrices.

To obtain the remaining projection matrices for all the views, we multiply the rotation matrix $\mathbf{R}$ by an incremental rotation matrix $\Delta\mathbf{R}$ as follows

$$\Delta\mathbf{R} = \begin{pmatrix} \cos\theta & 0 & -\sin\theta \\ 0 & 1 & 0 \\ \sin\theta & 0 & \cos\theta \end{pmatrix} \tag{A.4}$$

where $\Delta\mathbf{R}$ is an incremental rotation matrix, $\theta = 20^\circ$, the Y-axis of world coordinate coincides with the rotational axis of the turntable, the X-axis of world coordinate is located horizontally on the front face, and the Z-axis of world coordinate is pointed outward from the front face. Thus, the projection matrices for all the cameras cab then be generated by

$$\mathbf{P}_i = \mathbf{K}\left[\mathbf{R} * \Delta\mathbf{R}^{i-1} \quad \mathbf{t}\right] \tag{A.5}$$

where i=1 to 18 for our thermal reconstruction model.

Bibliography

[1] Jionghua Jin, Jianjun Shi, "Diagnostic feature extraction from stamping tonnage signals based on design of experiments," *Transactions of the ASME*, Vol. 122, Issue 2, pp. 360-369, May 2000

[2] Art Hedrick. (2002, Oct. 24). Taking advantage of simulation technology. *Stamping Journal* [Online]. Available: http://www.thefabricator.com/Articles/Stamping_Article.cfm?ID=138

[3] Li, Shaofan, W. Hao, and W. K Liu, "Numerical Simulations of large deformation of thin shell structures using meshfree methods," *Computational Mechanics*, Vol. 25, 2/3, pp. 102-116, 2000.

[4] Hyunbo Shim, Kichan Son, and Kwanghee Kim, "Optimum blank shape design by sensitivity analysis," *Journal of Materials Processing Technology*, Vol. 104, Issue 3, pp. 191-199, 2000.

[5] H.J. Antunez, "Thermomechanical modeling and sensitivity analysis for metal-forming operations", *Computer Methods Appl. Mech. Engrg.* 161, pp. 113-125, 1998.

[6] K.K. Choi, Nam H. Kim, Iulian Grindeanu, and JS Chen, "Die shape design optimization of sheet metal stamping process using meshfree method", *Intl. J. Numer,Meth.Engng*; 51:1385-1405, 2001.

[7] S. Kok, N. "Optimization of a sheet metal forming process using successive multipoint approximations", *Structural Optimization*, Vol. 18, Issue 4, 1999.

[8] Jansson T., Optimization of sheet metal forming processes, Thesis no. 986, LIU-TEK-LIC-2002:59, Linköping Institute of Technology, Linköping 2002.

[9] F. EL KHALDI and M. LAMBRIKS (2002). New requirements and recent development in sheet metal stamping simulation. Presented at NUMISHEET 2002. [Online]. Available: http://www.esi-group.com/Products/Stamping2G/publications_html.

[10] A. M. JOSHI. Formability studies on sheet metals. METAL WEB NEWS Technical report. [Online]. Available: http://www.metalwebnews.com/howto/sheet-metal/sheetmetal-study.pdf

[11] GOM. Optical metal sheet forming analysis. Gesellschaft für Optische Meßtechnik, Braunschweig, Germany. Technical report Available: www.gom.com/pub/publications/smf.pdf

[12] D.W. Manthey and D. Lee, "Vision-based surface strain measurement system," *JOM: The Member Journal of The Minerals, Metals and Materials Society*, 47(7): 46-49, 1995

[13] T. Schmidt and J. Tyson (2003, Feb.). Dynamic strain measurement using advanced 3D potogrammetry. Trilion Quality Systems, GOM mbH..[Online]. Available: http://www.gom.com/En/Applications/Deformation/pub/dynamic_strain.html

[14] J. L. M. Fernandes, J.M.C. Rodrigues, P.A.F. Martins , "Combined finite element-boundary element thermo-mechanical analysis of metal forming processes", *Journal of Materials Processing Technology*, Vol. 87, ,pp. 247-257, 1999.

[15] S. Khan, Sujian Huang, *Continuum Theory of Plasticity*, Wiley-Interscience Publication, 1995.

[16] R.H.Wagoner , J.-L.Chenot ,"Metal forming analysis" Cambridge University press.2001

[17] Kavesary S. Raghavan and R.H. Wagoner, "Combined influence of geometric defects and thermal gradients on tensile ductility", *Metallurgical transactions*. Vol. 18A , pp. 2143-2150, 1987.

[18] Robert A.Ayres , "Thermal gradients, strain rate, and ductility in sheet steel tensile specimens", *Metallurgical Transactions* Vol. 16A , pp. 37-43, Jan. 1985.

[19] R.H.Wagoner , J.-L.Chenot ,"Metal forming analysis" Cambridge University press.2001

[20] Xavier P.V. Maldague et al , "Infraed methodology and technology", *International advances in nondestructive testing* , Vol.17 , 1992

[21] Yong H. Kim and R.H. Wagoner, "An analytical investigation of deformation induced heating in tensile testing", *J. Mech .Sci,* Vol. 29 No.3, pp.179-194, 1987.

[22] R.Hill, "The mathematical theory of plasticity", Oxford university press, 1985.

[23] Chao C.K, Liu C.H and Wu H.J, " Numerical and failure analysis on the drawing of a circular cylindrical cup", *Engineering Fracture Mechanics*, Volume 45, Issue 4, pp. 439-450, July 1993.

[24] J. M. Barata Marques and R. M. S. O. Baptista " Theoretical and experimental analysis of axisymmetrical deep drawing",*Journal of Materials Processing Technology*, Vol. 24, Issue 1, pp. 53-63, December 1990.

[25] Mark Colgan, John Monaghan , "Deep drawing process: analysis and experiment", *Journal of Materials Processing Technology*, Volume 132, Issues 1-3, pp. 35-41, April 2003.

[26] Meinders T., Developments in numerical simulations of the real life deep drawing process, Ph.D. Thesis , University of Twente, Enschede, Ponsen & Looijen Wageningen (publ.), ISBN 90-36514002, 2000.

[27] S Thiruvarudchelvan, W Lewis, N H Loh ,and G K Gan, Deep drawing of cups of different shapes simplified with the use of Friction-induced Blank Holding Force. [Online] Available: http://www.ntu.edu.sg/home/mthiru/Friction/Friact.htm

[28] Yiu-Ming Harry Ng and R. Du, "Acquisition of surface thermal distribution in sheet metal forming," *Proceedings of the 11th IEEE International Conference on Mechatronics and Machine Vision in Practice*, no.32, Macau, China, 30 Nov.- 2 Dec., 2004.

[29] Y. –M. H. Ng and R. Du, "Reconstruction of 3D thermal distribution from infrared images," *Proceedings of the First Asia International Symposium on Mechatronics*, Xian, China, pp. 379-383, Sept. 2004

[30]R. Szeliski, "Rapid octree construction from image sequences," *Computer Vision, Graphics and Image Processing*, 58(1): 23-32, 1993

[31]W. Harvey Gray, C. Dumont and M. A. Abidi, "Integration of multiple range and intensity image pairs using a volumetric method to create textured 3D models," *Proc. of SPIE Conference on Machine Vision Applications in Industrial Inspection VII*, Vol. 3966, pp. 94-104, San Jose, CA, USA, Jan. 2000.

[32] J. -C. Nebel and et al, "3D thermography for the quantification of heat generation resulting from inflammation," *Proc. of 8th 3D Modelling Symposium*, Paris, France, 2003.

[33] J. -C. Nebel and et al, "3D thermography imaging standardization technique for inflammation diagnosis," *Proc. of SPIE Conference on Photonics Asia 2004*, Vol. 6, pp. 5640-5646, Beijing, China, Nov. 2004.

[34] Camera Calibration Toolbox for Matlab, http://www.vision.caltech.edu/bouguetj/calib_doc/

[35] K. –Y. K. Wong, "Structure and motion from silhouettes," *PhD dissertation, Department of Engineering, University of Cambridge*, 2001

[36] W. E. Lorensen, H. E. Cline, "Marching cubes: a high resolution 3D surface construction algorithm," *ACM Computer Graphics*, 21(4): 163-169, July 1987

[37] C. Montani, et al, "A modified look-up table for implicit disambiguation of marching cubes," *The Visual Computer*, 10(6): 353-355, 1994

[38] X. Huang, M. Hu, and E. Zhou, "Novel FEM method to compute 3D thermal distribution of electrical machine," *Proceedings of CSEE.*, Nanjing, China, vol. 18, no. 2, pp. 78-82, March 1998.

[39] X. Huang, D. Lu, and M. Hu, "New FEM method based on arch-shaped elements to compute 3D thermal distribution of electrical machine," *IEEE Power Engineering Society General Meeting*, pp. 1497 – 1499, Vol.2, June 2004.

[40] M. Hu, et al, "A novel FEM method to calculate 3D thermal distribution in the end region of turbo-generator and its application," *Proceedings of International Conference on Electrical Machines*, vol. 1, pp. 152-155, 2000.

[41] Y. Du, "Study of temperature distribution in the end region of large turbogenerators," *Proceedings of the CSEE*, vol. 16, no. 2, pp. 95-101, March 1996.

[42] D. Sarkar, P. K. Mukherjee, and S. K. Sen, "Use of 3-diemensional finite elements for computation of temperature distribution in the stator of an induction motor," *IEE Proceedings B Electric Power Applications*, vol. 138, issue 2, pp. 75-86, March 1991.

[43] T. Kataoka, and Y. Nakamura, "Prediction of thermal sensation based on simulation of temperature distribution in a vehicle cabin," Heat Trasfer – Asian Research, vol. 30, issue 3, pp. 195-212, 2001.

[44] J. Hinderer, "Model for generating synthetic three-dimensional (3D) images of small vehicles," *Proceedings of SPIE Conference on Infrared Sensors and Sensor Fusion*, vol. 782, pp. 8-13, 1987.

[45] C. Oh, N. Nandhakumar, and J. K. Aggarwal, "Integrated modelling of thermal and visual image generation," *Proceedings of IEEE Conference on Computer Vision and Pattern Recognition*, pp. 356-362, June 1989.

[46] J. Michel, and N. Nandhakumar, "Unified 3D models for multisensor image synthesis," *Graphical Models and Image Processing*, vol 54, no. 4, pp. 283-302, July 1995.

[47] British Turntable Co Ltd
http://www.driveawaymat.co.uk/

[48] K. Kutulakos, and S. Seitz, "A theory of shape by space carving," *International Journal of Computer Vision*, vol. 38, issue 3, pp. 199-218, 2000.